Serpentinization and H2 production during an iron-clay interaction experiment at 90C under low CO2 pressure

Régine Mosser-Ruck, Jérôme Sterpenich, N. Michau, Marie-Camille Jodin-Caumon, A. Randi, M. Abdelmoula, Odile Barres, Michel Cathelineau

Serpentinization and H_2 production during an iron-clay interaction experiment at 90°C under low CO_2 pressure

R. Mosser-Ruck[a*], J. Sterpenich[a], N. Michau[b], M.-C. Jodin-Caumon[a], A. Randi[a], M. Abdelmoula[c], O. Barres[a] and M. Cathelineau[a],

[a]Université de Lorraine, CNRS, GeoRessources, F-54000 Nancy, France

[b]ANDRA, 92298 Châtenay-Malabry Cedex, France.

[c]Université de Lorraine, CNRS, LCPME, F-54000 Nancy, France

*Email address of the corresponding author: regine.mosser@univ-lorraine.fr

Telephone number: 33(0)3 72 74 55 38; Fax number: 33(0)3 72 74 55 14

Abstract:

Interactions between steel canisters and clay-rich material in deep geological repositories for high-level nuclear waste were studied by reacting metallic iron and a claystone from the Callovo-Oxfordian formation of the Paris Basin (COx). The experiment ran at 90°C for 14 weeks in the presence of water and under 20 mbar of initial CO_2 partial pressure ($p(CO_2)$). At the end of the experiment, the pressure in the autoclave reached 50 bar due to H_2 production. Water was almost entirely consumed and poorly crystallized 7Å-greenalite-type clays were formed at the expense of illite and mixed-layered illite-smectite minerals (I/S). The dissolution of quartz and pyrite and the crystallization of pyrrhotite were also observed. Considering the results of Mössbauer and Fourier Transformed Infrared (FTIR) spectroscopies, iron carbonate and and/or ferrous hydroxycarbonate were suspected to precipitate but in very small amounts. A follow-up of the mineralogical evolution by XRD (X-ray diffraction), SEM (Scanning Electron Microscopy) and TEM (Transmission Electron

Microscopy) shows that serpentinization of clays (formation of greenalite) is accompanied by a significant consumption of water and the production of H_2 gas due to the oxidation and dissolution of metallic iron. Experimental results are in good agreement with geochemical modelling with the PHREEQC code. The kinetics of the iron corrosion was evaluated from H_2 production and shows that diffusion processes are the rate limiting step.

Keywords: serpentinization, iron-clay interaction, hydrothermal experiment, corrosion, H_2, geochemical modelling

1. Introduction

In the concept of high-level radioactive waste repositories, the claystone of the geological barrier could come into contact with alloyed or non-alloyed steel elements (liners of the disposal cells, waste containers and overpacks). Steel will be corroded in the presence of interstitial water coming from the geological formation and this reaction will produce iron-rich fluids and molecular hydrogen. The enhanced availability of Fe(II) resulting from this corrosion under reducing conditions will favor the transformation of some minerals in the claystone. Even if CO_2 (produced during oxidation of the claystone in the course of drilling of galleries and disposal cells) and H_2 (produced during corrosion of the steel in contact with the claystone) have already been identified in previous studies, their relationship with the mineralogical transformations of the claystone has been rarely investigated in recent research. A detailed "state of the art" concerning i) experimental iron-clay/claystone interactions, ii) effect of carbonates on iron corrosion and iii) serpentinization of silicates is thus detailed hereafter.

1.1 Experimental iron-smectite interactions

Over the last few years, numerous studies were dedicated to experimental investigations of iron-smectite or iron-bentonite interactions. They report the destabilization of smectite and the formation of various iron-rich phyllosilicates depending on temperature, pH, iron/clay and liquid/clay ratios. At temperature lower than 90°C and for high iron:clay (> 0.1) and liquid:clay (>1) mass ratios (Lantenois et al. 2005; Bildstein et al. 2006; Wilson et al. 2006b; Perronnet et al. 2008; Osaky et al. 2010; Mosser-Ruck et al. 2010; Pierron 2011 and Lanson et al. 2012, among others), the crystallisation of Fe-rich 1:1 phyllosilicates (serpentine group minerals) is observed instead of Fe-rich trioctahedral smectites or chlorites, the latter being favored by higher temperatures (Guillaume et al. 2003, 2004; Wilson et al. 2006a; Mosser-Ruck et al. 2010; Pierron 2011). Different studies of the influence of the chemical composition of smectite have also been carried out (Lanson et al. 2012; Lantenois et al. 2005; Perronnet et al. 2008) and showed a correlation between the Si/Al ratios of the initial smectite and the type of newly-formed 1:1 phyllosilicates, depending on the maturation of a Si-Al-Fe gel resulting from the destabilization of the initial smectite. Kaufhold et al. (2015) and Kaufhold and Dohrmann (2016) also reported that iron is less corroded in presence of Na-smectites compared to Ca-smectite or structural Fe-rich smectites. They concluded that both the layer charge density and the type of interlayer cation in smectite play an important role on the corrosive effect of this mineral (higher in presence of low charge smectites) and on the gel density and hence the solid/liquid ratio at the contact to the radioactive waste steel containers.

1.2 Experimental iron-claystone interactions

Studies concerning the interactions between iron and natural claystone are less numerous and the effect of the $p(CO_2)$ on mineralogical changes is rarely considered. Furthermore, certainly the form in which iron (and/or steel) is introduced into interaction experiments with clays (powder, foil, rods, etc.) plays a preponderant role both on the nature of the secondary phases

and the corrosion rate of iron. Newly formed minerals of the serpentine group, associated with the formation of magnetite, siderite and the dissolution of quartz, illite and interstratified illite/smectite are reported in experimental studies of iron corrosion (powder or foil) ± glass in contact with the COx claystone under an oxygen-free atmosphere and in the presence of pure water at 90°C during 6 to 18 months (De Combarieu et al. 2007, 2011). In the case of rods of low-allow carbon steel corroded at 90°C under anoxic condition in contact with the COx formation saturated with a synthetic clay porewater, the nature of the corrosion products can both depend on the duration of the experiment and the damage area at the C-steel/clay interface. Schlegel et al. 2019, reported the formation of Fe(hydr)oxide and (Fe,Si) (hydr)oxide phases, ankérite, akaganeite, later replaced by (Fe,Si,O) corrosion products containing Fe sulfide and chukanovite. Another original experimental procedure by step cooling from 90°C to 40°C (Pignatelli et al. 2013, 2014b) confirms without doubt, the formation of cronstedtite at 90°C, with an increase of crystallinity occurring from 90°C to 60°C, and the crystallization of chukanovite at the surface of iron plates (Pignatelli et al. 2014a). Specific surface area of metallic iron on the reaction pathway and its impact on corrosion rate and on Fe-enrichment of the clay particles, as well as the effect of a thermal gradient (150°C-300°C or 80°C-150°C) were also studied (Bourdelle et al. 2014; Jodin-Caumon et al. 2012). These studies demonstrate that the initial clay minerals, mostly illite and I/S, are replaced by chlorite, Fe-serpentine or mixed-layer smectite-(chlorite or serpentine) depending on the temperature.

1.3 Effect of bicarbonate/carbonate ions on iron corrosion processes

The knowledge of the $p(CO_2)$ in claystones is a key parameter to understand the thermodynamic equilibria governing the carbonate system. Gaucher et al. 2010, measuring the $p(CO_2)$ in four geological sites, demonstrated that it ranges between 3 mbar and 13 mbar and

that it is governed by an assemblage of calcite, dolomite and Mg-clay minerals. These values are higher than the atmospheric p(CO_2) (around 0.35 mbar) and favor the formation of iron carbonates as corrosion products when the claystone is in contact with steel elements in radioactive waste repositories. The wide variation in the nature of alteration products identified in numerous experiments is due to various experimental set-up defined to simulate the geochemical conditions in the storage (steel + groundwater ± clays or claystone ± CO_2 overpressure). For investigations carried out on iron corrosion and ferrous archaeological artefacts in the presence of carbonate-containing aqueous solutions and under anoxic conditions (Blengino et al. 1995; Savoye et al. 2001; Musić et al. 2004; Kohn et al. 2005; Refass et al. 2006; Saheb et al. 2008, 2009, 2010, 2011; Schlegel et al. 2008, 2010; Nishimura and Dong 2009; Lee and Wilkin 2010; Ruhl et al. 2011; Rémazeilles and Refait, 2009), the formation of siderite and/or $Fe^{II}(OH^-)_x(HCO_3^-/CO_3^-)_y$ species, sometimes identified as chukanovite is reported. However, the conditions of formation of these minerals are mostly described at 25°C, pH of 6.3-7 (Saheb et al. 2008; Ruhl et al. 2011) or 8.3-9.5 (Blengino et al. 1995; Refass et al. 2006; Nishimura and Dong, 2009) and up to 11 (Azoulay et al. 2012). The proportion of the newly-formed iron hydroxide-carbonate is controlled either by the $[CO_3^{2-}]/[OH^-]$ or $[Fe^{2+}]/[OH^-]$ ratios and its stability field would be reduced by a low carbonate activity (Azoulay et al. 2012). In the context of a nuclear waste repository, the corrosion of iron and/or low alloyed steel at the contact of water-saturated bricks of clay was also investigated under anaerobic conditions and in a solution representative of the pore COx water with a pH fixed to 7.3 and a HCO_3^- concentration of 1.6 mmol/kgw (Martin et al. 2008; Schlegel et al. 2008, 2010). From iron to claystone, various corrosion layers are observed: an internal thin layer of magnetite, an intermediate $Fe_2CO_3(OH)_2$ (chukanovite) layer, an outer layer of Fe-rich 7Å-phyllosilicates, and a transformed matrix layer containing siderite ($FeCO_3$). Microcrystalline chukanovite often mixed with other iron-rich minerals, is identified

126 in other studies reproducing the corrosion of steel containers (Saheb et al. 2008, 2010;
127 Nishimura and Dong 2009; Pignatelli et al. 2014a). In the experiments of Pignatelli et al.
128 (2014b), the $p(CO_2)$ is not measured but considered at equilibrium with carbonates of the
129 claystone, i.e. around 0.038 ± 0.02 bar according to an experimental test (Bourdelle et al.
130 2014) which is a value quite close to that of experiments at 80°C described by Gailhanou et
131 al. (2017).
132
133 **1.4. Serpentinization of silicates**
134 Two thermal fields (Lost City and Rainbow) were especially well studied (Charlou et al.
135 2002; Douville et al. 2002, Früh-Green at al. 2003, Kelley et al. 2005; Fu et al. 2007;
136 Foustoukos et al. 2008) and demonstrated that hydrothermal alteration of ultramafic rocks at
137 mid-ocean ridges involves H_2 production because of the reduction of water together with the
138 oxidation of ferrous iron in olivine and/or pyroxene. Magnetite and magnesium hydroxides
139 are the by-products of this reaction. The hydrothermal source of H_2 attracted much attention
140 in recent years and both experimental studies and thermodynamic modelling were developed
141 to improve our understanding of the influence of different parameters (such as temperature,
142 pressure, water/rock ratio, availability of silica, partitioning and oxidation state of iron) on
143 this mineralogical transformation (Allen and Seyfried 2003, Seyfried et al. 2007; MacCollom
144 and Bach 2009; Klein et al. 2009; Marcaillou et al. 2011; Andreani et al. 2013).
145 Serpentinization mechanisms are also evoked in the case of CM chondrites to explain the
146 formation of cronstedtite (Pignatelli et al. 2016 and 2017). However, unlike the reactions
147 taking place in hydrothermal fields, the serpentinization of olivines or pyroxenes in chondrites
148 requires a large contribution of ferrous iron and water. This extraterrestrial environment is
149 after all closer to that of the experiment described below.

150 The study presented here measures the H_2 production and the effect of a low $p(CO_2)$ on the
151 formation of newly-formed iron-rich minerals (silicates, carbonates), during the corrosion of
152 iron under experimental conditions close to that of a nuclear waste repository and using a low
153 solution/COx ratio. The experiment was carried out at 90°C in the presence of pure water and
154 $NaHCO_3$ to produce a $p(CO_2)$ about 20 mbar. This value of $p(CO_2)$ is chosen from the
155 geochemical calculations with the PHREEQC code by Bourdelle et al. (2014) in their study of
156 iron-clay interactions under hydrothermal conditions. This value is also close to the maximal
157 $p(CO_2)$ modelled by Gaucher et al. (2009) for the Bure pore water (15.8 mbar). The total
158 pressure was monitored throughout the experiment. The minerals and the composition of the
159 gas phase were analysed to identify the reaction processes involved in the conditions of steel
160 corrosion of nuclear waste repositories. Geochemical modelling was performed to decipher
161 the reaction path followed by the system during the experiment.
162

163 **2. Materials and experimental conditions**

164 **2.1. Geological reactant**

165 The claystone comes from the Callovo-Oxfordian formation (COx) in the underground
166 research laboratory of Andra (Bure, France, borehole EST 26457 FOR1118) located in the
167 east of the Paris basin. The sample was taken in a borehole in the maximum claystone zone.
168 According to different authors (Rousset 2001; Gaucher et al. 2004, Rivard 2011), the
169 claystone is composed of 41 wt% to 44 wt% of clay minerals (illite and mixed-layered
170 illite/smectite as predominant clay minerals, and minor amounts of kaolinite and chlorite), 21
171 wt% to 25 wt% of quartz, 27 wt% to 31 wt% of carbonates (calcite and minor dolomite), with
172 the remaining proportions made up of pyrite, phosphates, K-feldspar and organic matter.
173 Claystone was ground to 40 µm and stored in a glove box under Ar. Iron was used as a
174 powder (< 50 µm, Riedel-de-Haën, purity> 99.5%) and as plates (Sigma-Aldrich, thickness

0.25 mm, > 99.99%). The reactants were mixed in pure Milli-Q water (18.2 MΩ.cm). $NaHCO_3$ powder (Sigma-Aldrich, > 99.7%) was added to buffer the initial $p(CO_2)$ (cf. below).

2.2. Experiment

The starting mixture was made up of 55.5 g of ground claystone and 55.5 g of iron powder. Three iron plates (~ 200 mg) were also placed at the bottom of the stainless steel reactor. The liquid/rock and the $iron_{(powder)}$/claystone ratios were equal to unity. Claystone and iron reacted at 90°C during 107 days in a polytetrafluoroethylene (PFTE) foil placed to protect the reactor from corrosion. The total volume of the reactor was 170 cm^3. The pressure was monitored by a calibrated pressure transducer (± 0.25 bar). The device was heated using a MICA heater band. The temperature was controlled by a thermocouple (± 1°C) set in a stainless steel thimble dipping into the autoclave. The temperature and pressure data were recorded every three minutes throughout the experiment. Ten milligrams of $NaHCO_3$ were added to the mixture to obtain a $p(CO_2)$. Indeed, at T > 70°C, the decomposition of $NaHCO_3$ yields CO_2 in agreement with the following reaction (1):

$$2\ NaHCO_{3\ (powder)} \rightarrow Na_2CO_{3(solid)} + H_2O_{(g)} + CO_{2(g)} \qquad (1)$$

The mass of $NaHCO_{3\ (powder)}$ added in the experimental medium allowed to reach a pressure of ~ 20 mbar at the beginning of the experiment. This value was estimated from (i) the free gas volume in the reactor after filling it with claystone, iron and water (around 86 cm^3), (ii) the fraction of CO_2 dissolved in water at 90°C (estimated at around 10% of CO_2(g) produced).

3. Analytical techniques and geochemical modelling

3.1. Solid analysis

198 FTIR and Mossbauer spectroscopies, XRD, TEM and SEM analytical techniques are
199 described in Mosser-Ruck et al. (2010, 2016).

200 **3.2. Gas analysis**

201 The gases were collected in a cell equipped with a sapphire window and analysed by Raman
202 spectrometry. Raman spectra of the gaseous phase were recorded using a RXN1 Raman
203 spectrometer (Kaiser Optical Systems, Inc.) equipped with a 532 nm Nd:YAG laser at 80
204 mW, a multiplex holographic grating, and a CCD detector cooled to - 40°C by the Peltier
205 effect. The spectral resolution was of ~ 3 cm^{-1} at 1400 cm^{-1}. The Raman spectra were acquired
206 using 20x objective (Olympus) to focalize inside the cell and connected to the spectrometer
207 through an optical head and an optical fiber.

208 **3.3. Geochemical modelling**

209 Thermodynamic equilibria and reaction paths were calculated with the PHREEQC
210 geochemical code (Parkhurst and Appelo 1999) using the
211 ThermoChimie_PHREEQC_SIT_v9b0 database of Andra (Giffaut et al. 2014). The data base
212 using the SIT theory (Specific ion Interaction Theory) for the calculation of aqueous species
213 activities was chosen because of the high ionic strength expected in our system (I≈1.6
214 mol/kgw). Carbonates under reducing conditions in the presence of H_2 can transform to CH_4
215 but this reaction is kinetically unfavorable and furthermore CH_4 remained undetected by
216 Raman spectroscopy in our experiment. In consequence, thermodynamic data concerning CH_4
217 were removed of the database before calculations of the modelling in order to avoid the
218 formation of CH_4. The first step of the modelling was to mix COx with water at 90°C to
219 determine the mineral phases expected to crystallize (saturation index $SI \geq 0$). Among these
220 phases, those observed in the experiment and others not observed but relevant in the context
221 were allowed to crystallize and thus added to the input file. Table 1 shows the input file for

222 modelling, which includes the following data: i) minerals initially present in the COx sample
223 (according to the mineralogical determination of Rivard 2011) and considered as reactive; ii)
224 secondary minerals allowed to precipitate, including those likely to crystallize at 90°C (Fe(s),
225 cronstedtite-Th, greenalite, siderite, gibbsite, magnetite, nontronite-Ca, saponite-FeCa,
226 pyrrhotite). No zeolites were added to the list of secondary minerals because when tested in
227 the modelling, only phillipsite-K crystallized in the first step of the modelling and led to the
228 dissolution of all the initial clays of the COx. This result was not consistent with the
229 observations on the experimental products; iii) the water chemistry. The aqueous solution
230 contained 2.14 mmol/kgw of Na^+ and HCO_3^- to simulate the addition of $NaHCO_3$ in the
231 experiment. The number of moles for each mineral was recalculated for 1 kg of COx, and iron
232 (as Fe^0) was added step by step to 18 moles (~ 1 kg of iron), to mimic a reaction pathway. The
233 amount of iron added at each step was small at the beginning of the modelling (0.01 mole to
234 0.1 mole) when mineral transformations were more sensitive to iron content, and then
235 increased progressively until the total quantity of iron in the experiment was attained (18
236 moles). Because of its high reactivity, iron added at each step is completely dissolved before
237 proceeding to the next iteration (additional iron step) in the modelling. pH and pe (negative
238 log of the conventional activity of the electron) were free to vary. The temperature was fixed
239 at 90°C. Solid-solutions and ion exchange were not considered by the simulation program.

240

Mineralogical composition of the COx (1 kg)		Secondary minerals	Starting solution (1kg H_2O)*
Quartz	3.49 Mol	Fe(s)	
Calcite	2.3 Mol	Cronstedtite-Th	
Dolomite	0.216 Mol	Greenalite	
Illite_Imt-2	0.45 Mol	Siderite	
Illite/smectiteISCz-1	0.64 Mol	Gibbsite	Na: 2.14 mMol
Pyrite	0.25 Mol	Magnetite	HCO_3^-: 2.14 mMol
Ripidolite_cCa-2	0.036 Mol	Nontronite-Ca	
Kaolinite	0.11 Mol	Saponite-FeCa	
		Pyrrhotite	

241

242 **Table 1**: Data of the input file for the thermodynamic simulation of the experiment.* Salts in
243 the natural interstitial water of COx are not taken into account in the modelling

244 **4. Results**

245 **4.1. Pressure monitoring**

246 Before heating, a vacuum was created in the reactor to remove air and especially oxygen. The
247 pumping step was almost instantaneous (several tens of seconds) to obtain a vacuum of 0.01
248 bar avoiding massive water evaporation. Notice that at room temperature the evaporation rate
249 of water is low and the estimated amount of removed water is negligible (about 10^{-4} mole for
250 a saturated vapour pressure of 0.032 bar at 25°C). After ten minutes, the temperature reached
251 88°C and the pressure was equal to 0.73 bar, which is roughly the saturated vapour pressure
252 of pure water. In half a day, the pressure reached 1.93 bar. This result implies that the
253 experimental mixture quickly reacted. A pressure of 6 bar was reached within three days,
254 rising to about 50 bar at the end of experiment. This increase in pressure was due to the
255 production of gas by chemical reactions between the different components in the autoclave.
256 The Raman spectrum showed only H_2 bands while CO_2 remained below the limit of detection
257 (~0.5 bar).

258 **4.2. Mineralogical evolution**

259 Figures 1a and 1b present the diffractograms of the initial starting mixture and the reaction
260 product. The comparison of the two diffractograms in Fig. 1a shows that carbonate minerals
261 (calcite and dolomite) were apparently not very reactive. During the experiment, neither
262 magnetite nor iron-rich TOT or TOTO clays (e.g. minnesotaite, griffithite, bowlingite,
263 nontronite and chamosite) crystallized in sufficient quantity to be detected by X-ray
264 diffraction. On the other hand, dissolution of iron, quartz and clays (mainly I/S and illite)
265 were observed (Fig. 1a and Fig. 1b). 7Å-clay phases and chlorite were still present but always

266 in small proportions. However, the modifications of the mineralogical proportions have to be
267 considered with caution due to possible bias during sampling operations (heterogeneous
268 material). The diffractogram of the fine fraction of the reaction product (clay fraction < 2 µm)
269 shows peaks with a weak intensity (multiplication factor x5000), indicating a low crystallinity
270 of the clays.

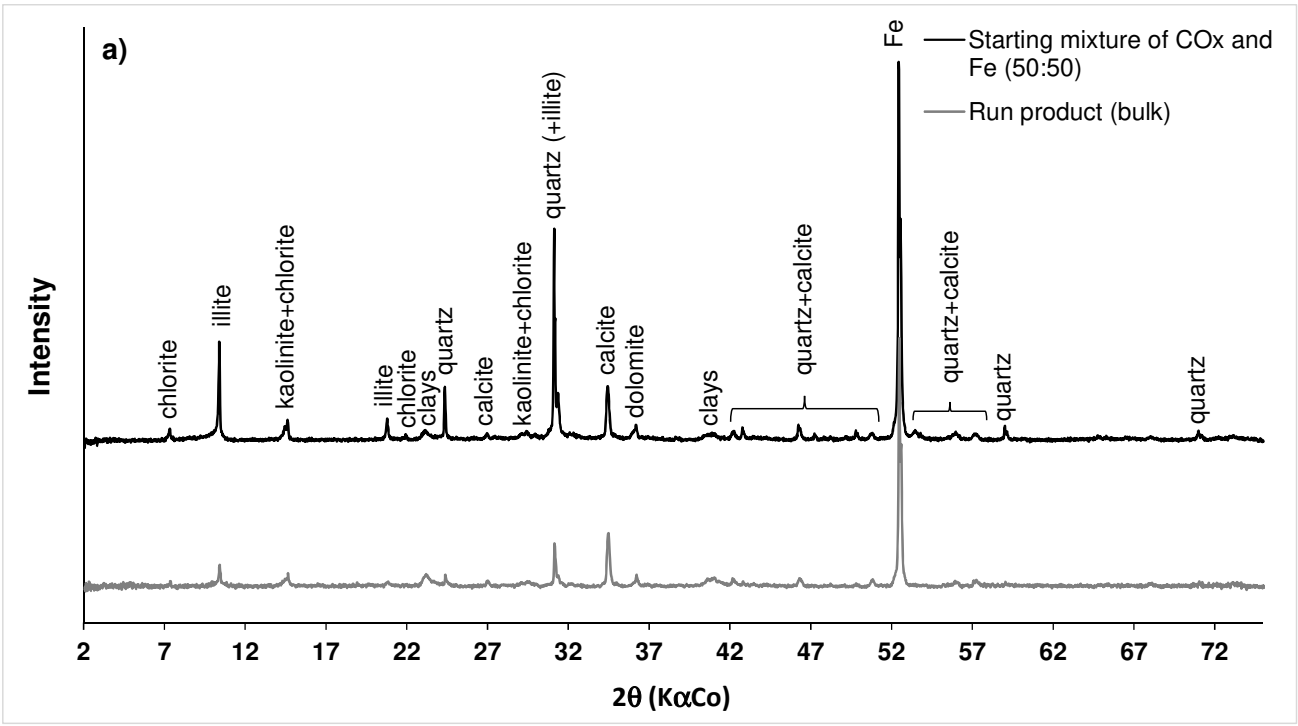

271

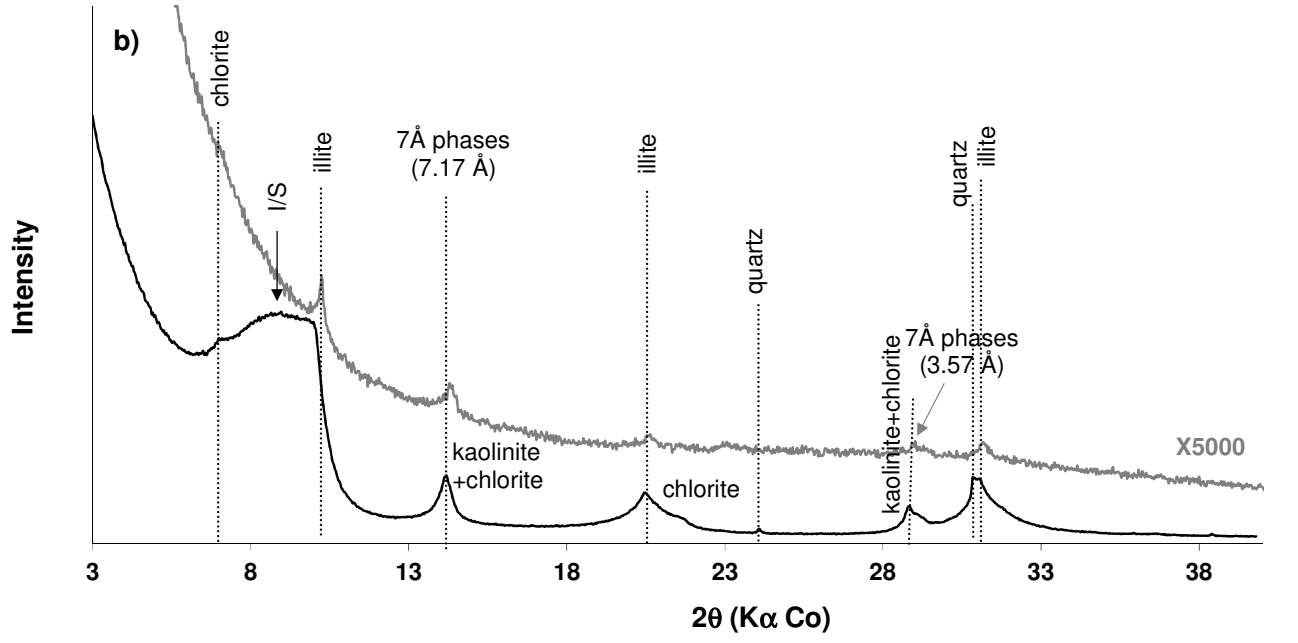

272

Fig. 1: a) Diffractograms of the starting mixture of claystone and Fe (black) and of the run-product (grey). b) Diffractograms of the air-dried oriented clay fractions (<2 μm) of the starting claystone (black) and of the run-product (grey). A multiplication factor (×5000) is applied to the diffractograms of the fine fraction of the reaction product for sake of clarity.

Figure 2 shows the chemical compositions of clay particles analyzed by TEM-EDXS (Energy-Dispersive X-ray Spectroscopy) in the initial claystone and in the reaction product. Iron is considered as Fe(II). A well-marked evolution was observed: i) silicon depletion coupled with a decrease of the interlayer charge (Fig. 2a), ii) a decrease of the interlayer charge correlated with the release of potassium (Fig. 2a and Fig. 2c), iii) a substantial enrichment in iron explained by a replacement of aluminum and magnesium in the octahedral sites (Fig. 2b). Iron enrichment and silicon depletion argue in favor of a transformation of I/S (± illite) minerals of the starting COx into chlorite or 7Å iron-bearing serpentines (Fig. 2d). The clay particles sampled in the bulk and from the iron plates in the reaction product cover a wide range of chemical compositions. Figure 3 shows that their mineral composition changes from interstratified clays (I/S) and/or illite to greenalite. These new argillaceous phases were interpreted as a mixture of dioctahedral and trioctahedral clays and/or complex mixed-layer clays, more or less enriched in iron and generally depleted in aluminum and potassium. The iron enrichment in the newly-formed clay particles probably depends on the distance from the iron source: it was higher in the clay particles collected close to the iron plates or close to iron powder.

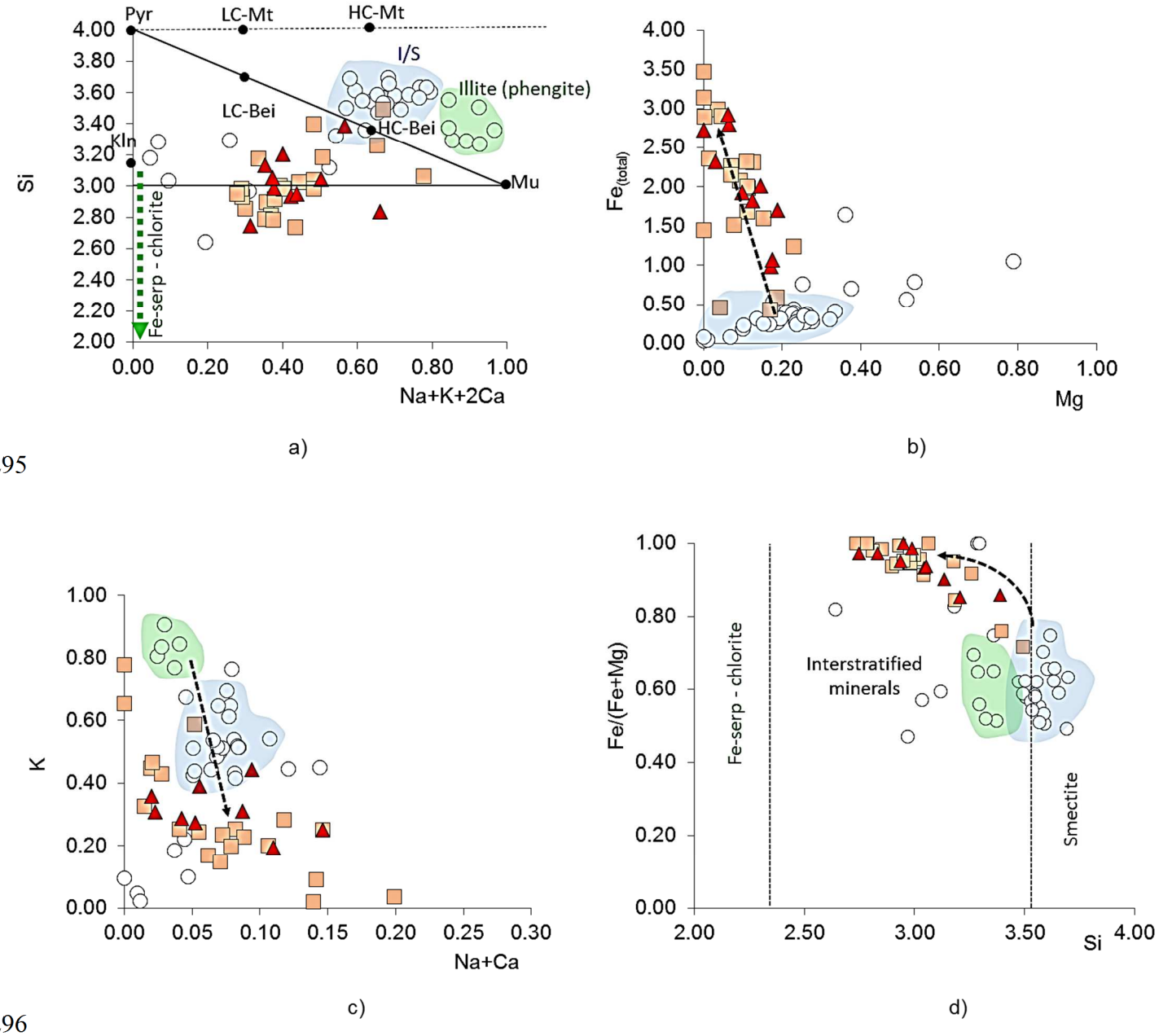

295

296

297 **Fig. 2**: Chemical compositions of clay minerals analyzed by TEM-EDXS in the COx starting
298 material (white circles) and the reaction product (orange squares for clay particles collected in
299 the bulk and red triangles for those collected on the iron plates). Spectra were collected under
300 nanoprobe mode, using a counting time of 40 s over an area of ~10 nm in diameter. Elemental
301 compositions were calculated assuming the thin film criteria (SMTF program: semi-
302 quantitative metallurgical thin film program) and using k-factors calibrated with
303 independently analyzed macroscopic micas, with a maximum error of 5% for each element.

304 Formula are calculated on the basis of 11 oxygens and represented in atoms per formula unit
305 (a.p.f.u.) in four binary diagrams. a) Si vs I.C. (I.C.=K+Na+2Ca); b) FeT (total Fe) vs Mg; c)
306 K vs Na+Ca; d) Fe/(Fe+Mg) vs Si. Reference minerals are: Kaolinite: Kln: $Si_4Al_4O_{10}(OH)_8$;
307 Muscovite: Mu : $Al_2(Si_3Al)O_{10}(OH)_2$ K; Pyrophyllite: Pyr : $Al_2(Si_4)O_{10}(OH)_2$;
308 Low-Charge Montmorillonite: LC-Mt: $(Al_{1.67}R^{2+}_{0.33})(Si_4)O_{10}(OH)_2M^{+}_{0.33}$; High-Charge
309 Montmorillonite: HC-Mt: $(Al_{1.33}R^{2+}_{0.67})(Si_4)O_{10}(OH)_2M^{+}_{0.67}$; Low-Charge Beidellite: LC-Bei:
310 $Al_2\ (Si_{3.67}Al_{0.33})O_{10}(OH)_2\ M^{+}_{0.33}$; High Charge Beidellite: HC-Bei: $Al_2\ (Si_{3.33}Al_{0.67})O_{10}(OH)_2$
311 $M^{+}_{0.67}$; Chlorite: $(R^{2+}_3)O_{10}(OH)_2\ (R^{2+}_{3-x}R^{3+}_x)(Si_{4-x}Al_x)(OH)_6$ with $0\leq x\leq 2$ et $0\leq FeT\leq 6$; Fe-
312 serpentine : Fe-Serp (greenalite, berthierine, cronstedtite). The dotted arrows indicate the
313 direction of the transformations.
314
315

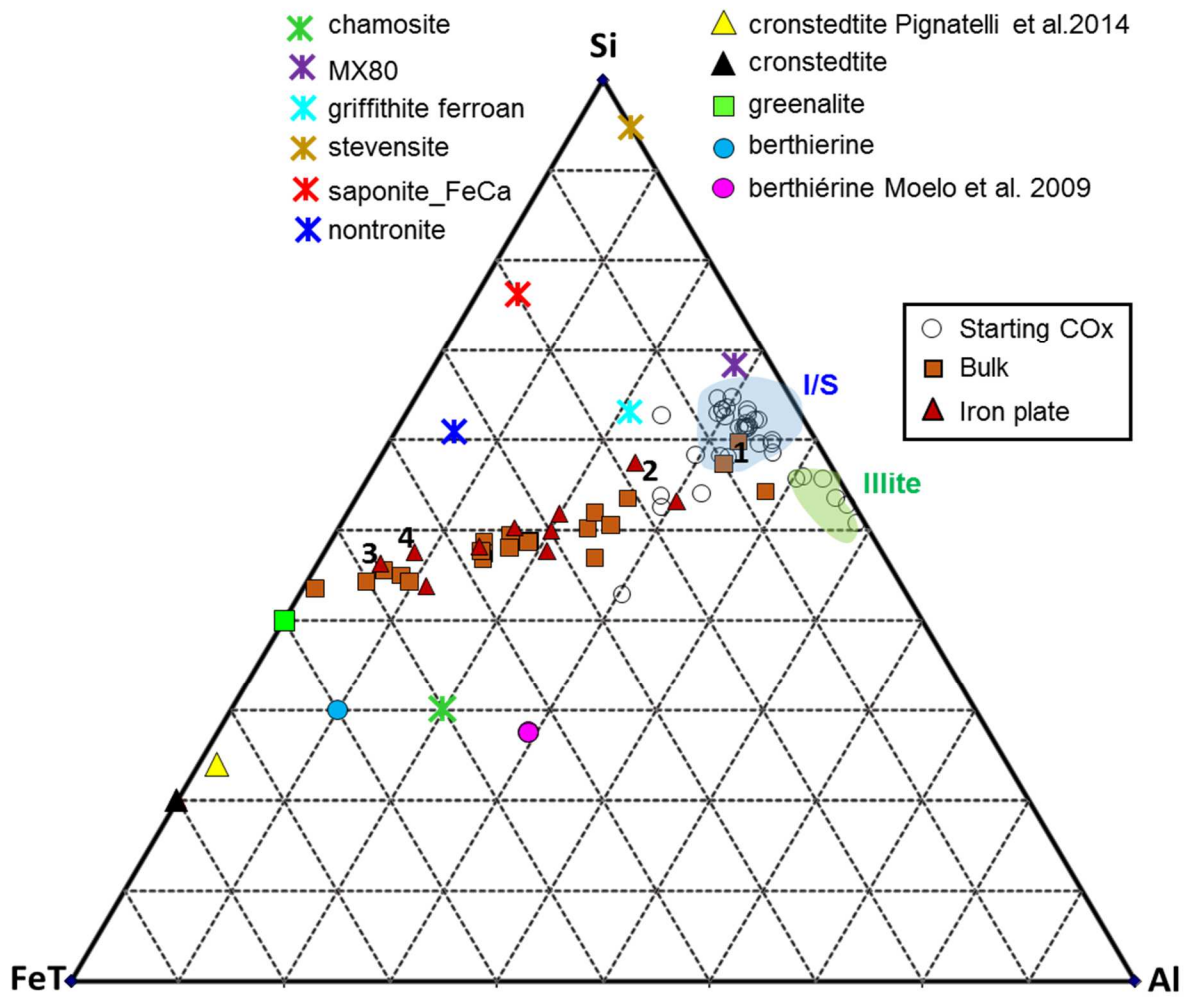

316

317 **Fig. 3**: Chemical compositions of clays in the reaction product (orange squares for clay
318 particles collected in the bulk, and red triangles for clay particles collected more or less close
319 to the iron plate), compared to the compositions of the clay minerals of the starting COx
320 (white circles). Formulae are calculated on the basis of 11 oxygens in the diagram Si-
321 FeT(totalFe)-Al. I/S: interstratified illite/smectite. Reference minerals (half formula) are:
322 Chamosite (green star): $(Fe^{2+}_3)(Fe^{2+}_2Al)(Si_3Al)O_{10}(OH)_8$;
323 Greenalite (green square): $(Fe^{2+}_3)(Si_2)O_5(OH)_4$;
324 Cronstedtite (black triangle): $(Fe^{2+}, Fe^{3+})_3(Si\ Fe^{3+})O_5(OH)_4$;
325 Berthierine (blue circle): $(Fe^{2+}, Fe^{3+})_3(Si_{1.5}\ Al_{0.5})O_5(OH)_4$;
326 MX80 (purple star): $(Al_{1.55}Fe_{0.17}, Mg_{0.28})(Si_{3.98}Al_{0.02})O_{10}(OH)_2\ Na_{0.18}\ Ca_{0.1}$, n H_2O;
327 Griffithite-ferroan (blue star): $(Fe^{2+}_{0.75}, Mg_{2.25})(Si_3Al)O_{10}(OH)_2\ Na_{0.1}\ Ca_{0.1}$, 4 H_2O;

328 Stevensite (brown star): $(Fe^{2+}_{0.2,}Mg_{2.8})\ (Si_4)O_{10}(OH)_2\ Na_{0.33}\ Ca_{0.15},\ 4\ H_2O$;

329 Saponite-FeCa (red star): $Fe^{2+}Mg_2\ (Si_{3.66}Al_{0.34})O_{10}(OH)_2\ Ca_{0.17},\ n\ H_2O$;

330 Nontronite (blue star): $(Fe^{3+})_2\ (Si_{3.7}\ Al_{0.3})\ O_{10}(OH)_2\ Na_{0.3}$

331 1, 2, 3 and 4 are the compositions of the clay particles shown on the TEM images of the Fig.
332 4.

333

334 In fact, two main morphologies were observed both in the bulk and near the iron plate. The
335 first morphology "cornflakes"-like, is typical of little transformed clays and weakly enriched
336 in iron (points 1 and 2 of Fig. 3). It was visible on TEM images a) and b) of Fig. 4. The
337 second morphology appeared as a "hairy" assemblage of small tabular particles (TEM images
338 b) and c) of the Fig.4), already observed by other authors (Bourdelle et al. 2014). These
339 particles are then very enriched in iron (points 3 and 4 of Fig.3).

340

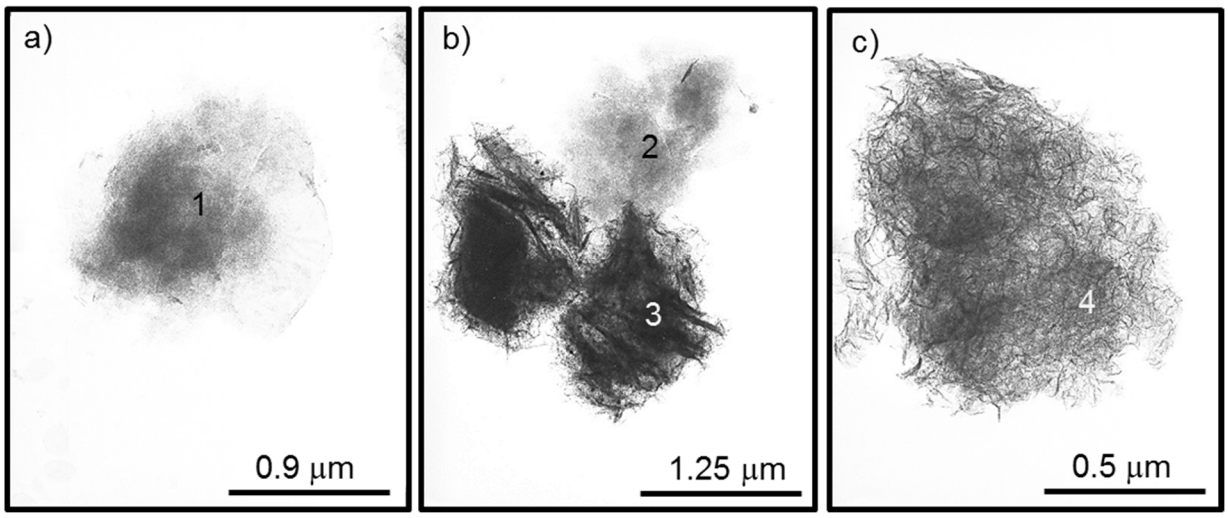

341

342 **Fig. 4**: TEM images of fine clay particles (<2 µm) recovered in the bulk (image a) and near
343 the iron plate (images b and c). Points 1, 2, 3 and 4 indicated the particles analyzed and
344 referred to the compositions plotted in the diagram of Fig. 3.

345 The iron plates used in the experiment were observed by SEM. The detailed examination of
346 the surface of the plates shows a great heterogeneity of the newly-formed mineralogical

phases. This was explained by a wide variety of contacts between the COx and the iron plate, the claystone being itself very heterogeneous. Fig. 5a shows a superposition of at least two different mineral layers on the iron plate. A first relatively homogeneous layer of smooth and cracked appearance (Fig. 5b) is composed of silicates (Fig. 5c) characterized by an iron enrichment (Fig. 5d). Some of the clay particles on the iron plate are well crystallized, with a polygonal platy morphology (see particles in the white squares of Fig.5c).

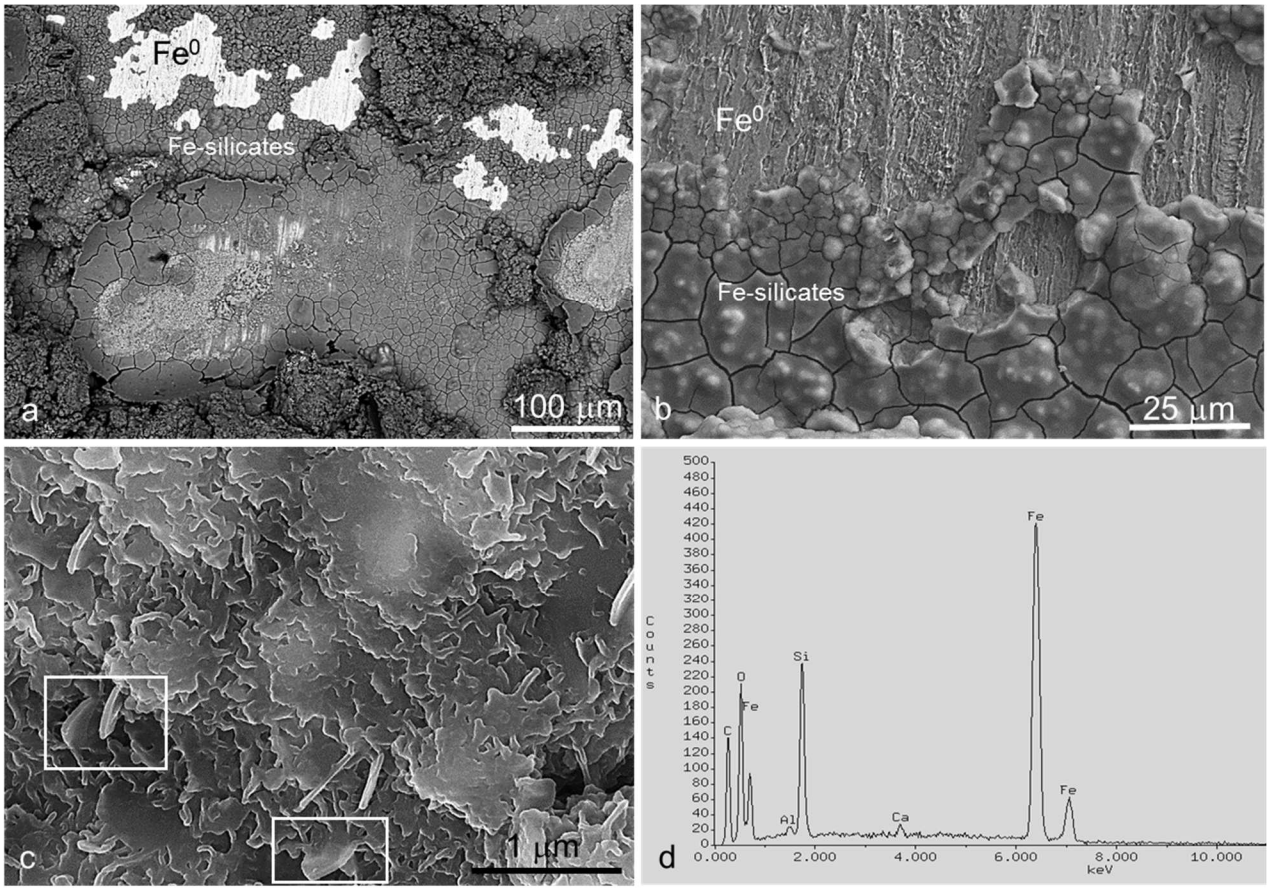

Fig. 5: SEM images in secondary electron mode and backscattered electron mode of the surface of the iron plate (a and b). Both images and spectrum were recorded with an accelerating voltage of 15 kV and a beam current of 10 nA. White rectangles on (c) indicate well crystallized iron-rich silicates with a polygonal platy morphology and (d) correspond to their EDXS analysis.

On other parts of the iron plate, iron silicates gather as a cellular assemblage, and other minerals are observed side by side (Fig. 6a). These last minerals are mainly composed of Fe and S in proportions close to those of pyrrhotite (Fig. 6b). Meanwhile, pyrites most often occur in the form of highly corroded framboids. The transformation of pyrite into pyrrhotite was already demonstrated at hydrogen pressures exceeding 30 bar (Jodin-Caumon et al. 2010 and Truche et al. 2013). After ultrasonic cleaning to eliminate clay particles, the iron powder also shows corrosion traces but no characteristic octahedral crystals of magnetite are observed either in the bulk or on the iron plates of the reaction product. Other minerals resulting from the corrosion of iron (iron oxy-hydroxides, ferrihydrite or other iron silicates) were not detected by the techniques used in this study maybe because of very low abundances.

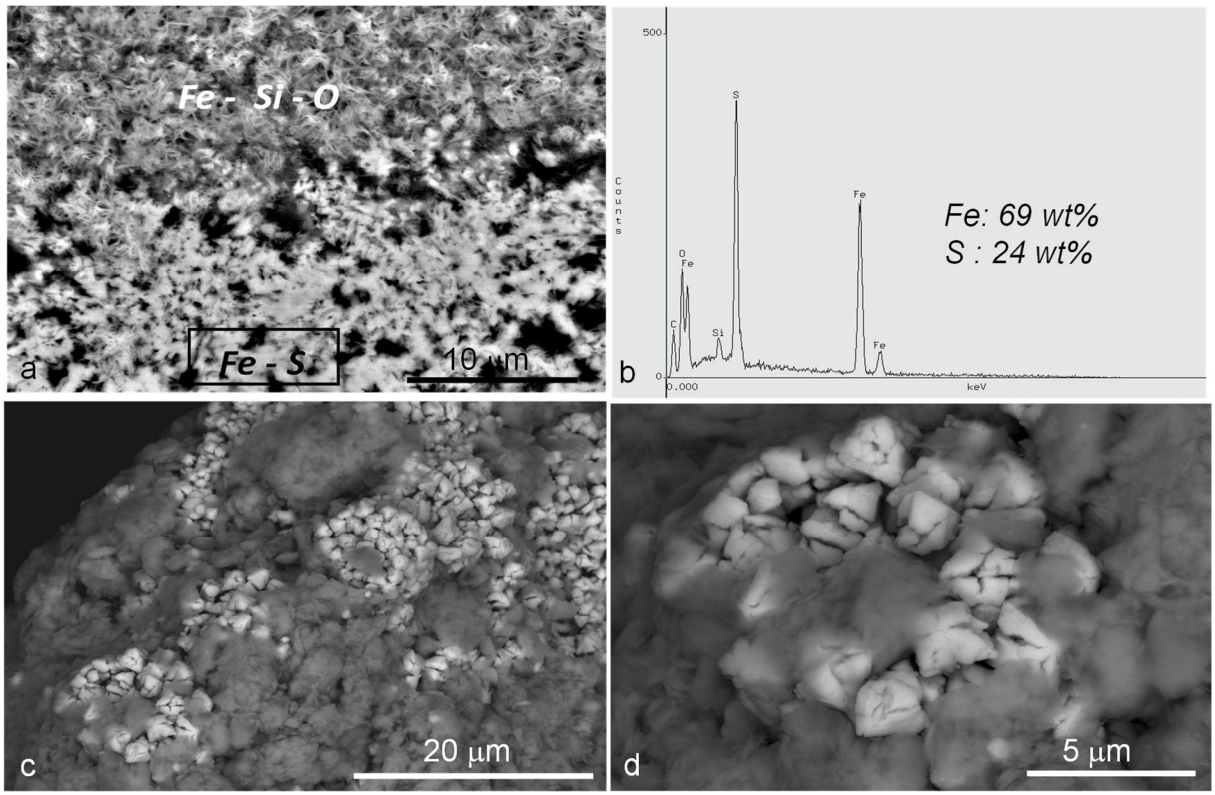

Fig. 6: (a): SEM image in backscattered electron mode of iron plate covered with iron silicates close to iron sulphides interpreted as pyrrhotite from EDXS analyses (b). (c) and (d) : corroded pyrite framboids. Both images and spectrum were recorded with an accelerating voltage of 15 kV and a beam current of 10 nA.

375 The characterization of the mineralogical assemblages of the reaction product by Mössbauer
376 spectroscopy was recorded in the ±11 mm/s velocity range because this was ideally suited to
377 distinguish iron in the clay minerals (paramagnetic doublets) from metallic iron or iron oxides
378 (Rivard et al. 2015). The fitting of the spectra was reasonably described in terms of a
379 magnetic contribution corresponding to metallic α-Fe in addition to a superimposition of
380 elemental subspectra (paramagnetic components): two doublets assigned to Fe^{3+} and Fe^{2+}
381 clays (53% and 7.5%, respectively) and a doublet characterized by a centre shift and
382 quadrupole splitting (1.08 mm/s and 1.98 mm/s) which correspond to Fe^{2+} in siderite (2.5%)
383 (Figure 7a). The high percentage of Fe^{3+} in the clays is surprising, and was explained by the
384 presence of original inherited clays (illite or chlorite) of the claystone which would have not
385 reacted and did not transform into Fe^{2+}-rich clays. The influence of atmospheric water and
386 carbon dioxide was always subtracted. Few differences between the spectra obtained from the
387 starting COx and the reaction product are observed (Fig. 7b). In the reaction product, FTIR
388 spectroscopy showed that quartz and carbonates (calcite) are still present as well as clays. But
389 clays are less hydrated than those of the starting claystone. A magnification between 1000 cm^{-1}
390 and 600 cm^{-1} (Fig. 7c) highlights that most of the infrared bands in the 600-950 cm^{-1} region,
391 characteristic of OH bending modes of clays are hidden in the background noise. The new
392 band at 630 cm^{-1} could be attributed to the bending vibration of OH of the hydroxide sheet in
393 the serpentine-like minerals and the small shoulder at 737 cm^{-1}, only visible on the spectrum
394 of the reaction product (Fig. 7c), could correspond to the stretching band of siderite (Farmer
395 1974).
396

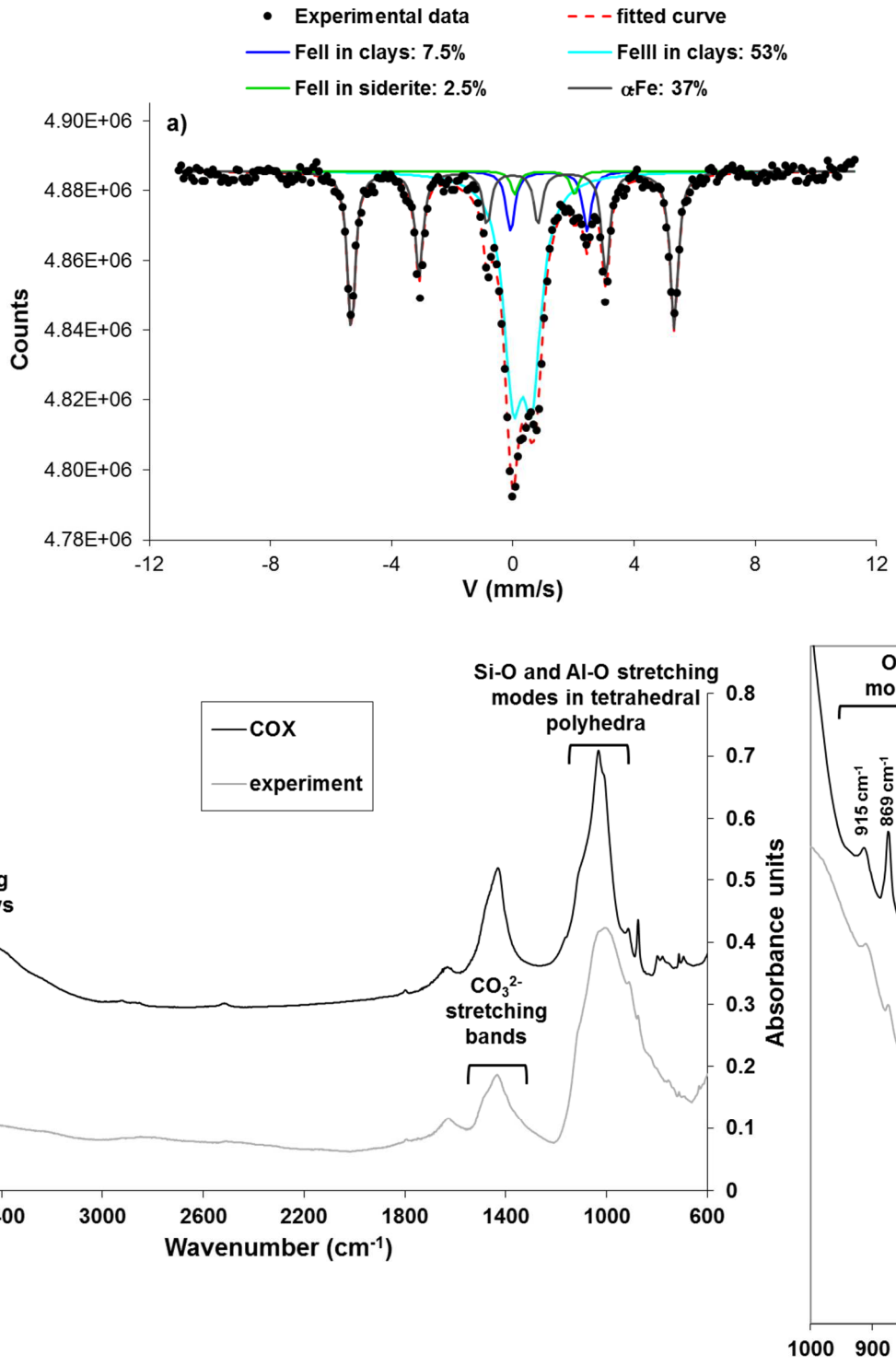

Fig. 7: a) Room temperature Mössbauer spectrum of the reaction product (bulk) in velocity range of ± 11 mm/s. The uncertainty about the relative abundances of iron in the different phases is ± 2%. b) FTIR spectra in transmission mode recorded on pellets of the COx starting material and of the reaction product (collected on the iron plates). Analyses were made using 1 mg of powder sample with 150 mg of pure potassium bromide (KBr) and were scanned for

about 2 minutes with a 2 cm^{-1} spectral resolution. c) Magnification between 1000 cm^{-1} and 600 cm^{-1}.

4.3. Geochemical modelling

Variations in pH and pe (Fig. 8a) indicate that the reaction medium becomes alkaline (up to pH ~11.6) and reduced (pe around -12.9). The modelling predicts that 54% (by mass) of water is consumed by both iron corrosion and mineralogical transformations (Fig. 8b).

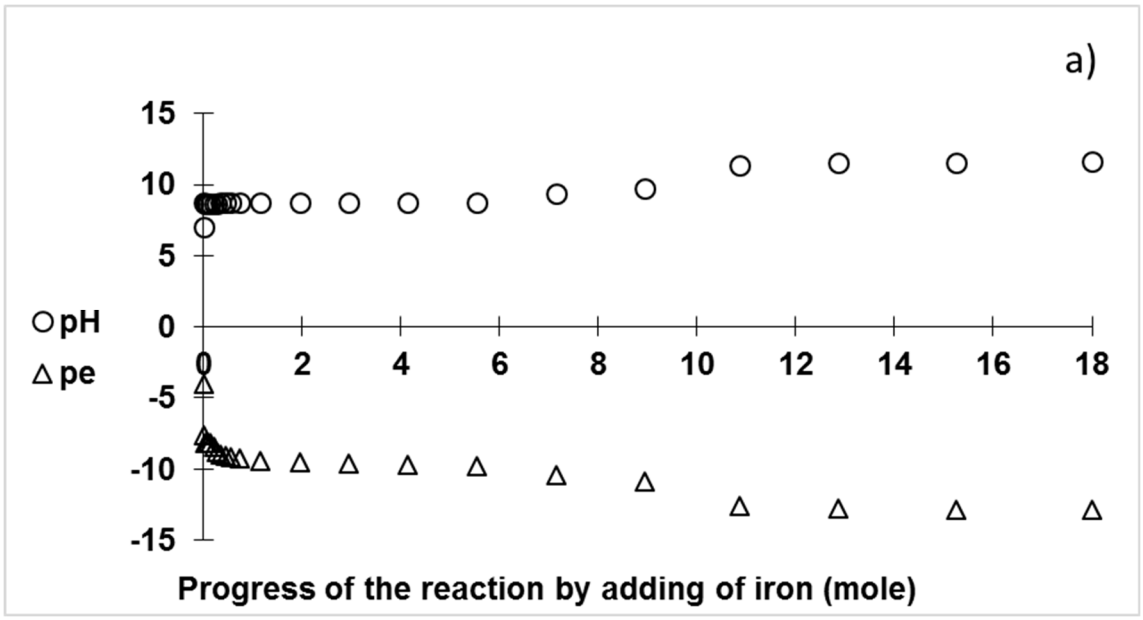

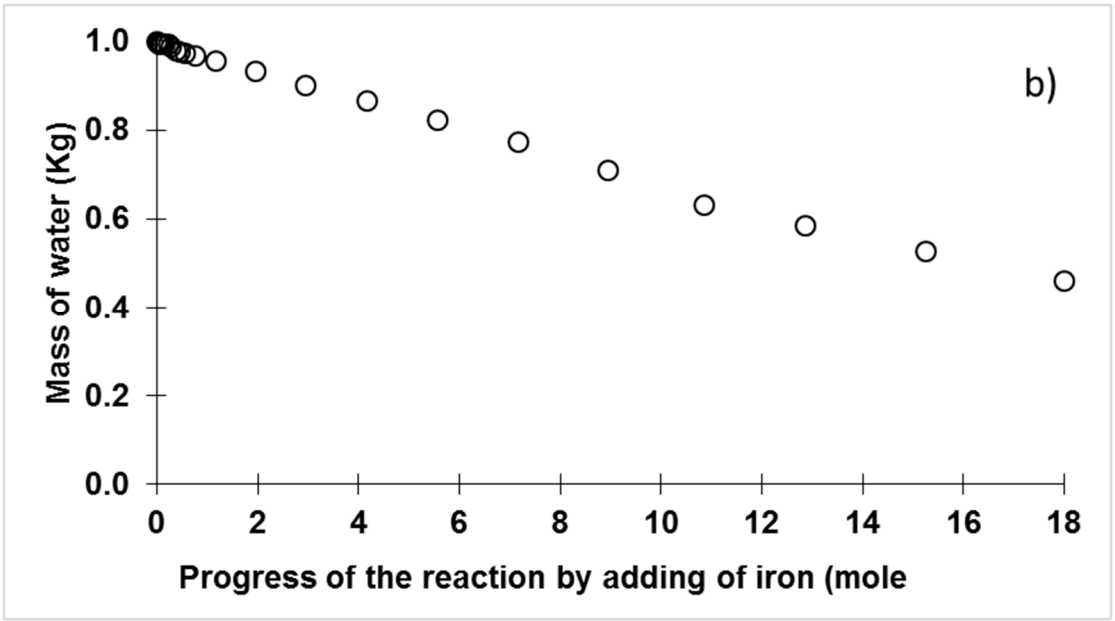

Fig.8: a) Evolution of pH, pe, b) evolution of mass of water consumed, versus the amount of iron introduced step by step during the PhreeqC modelling.

The modelling also highlights several points (Fig. 9a and Fig.9b): i) siderite, cronstedtite and nontronite-Ca do not crystallize, ii) at the first steps of iron addition (<0.4 mole), calcite, quartz, kaolinite, saponite-FeCa, illite and pyrrhotite crystallize whereas ripidolite_Cca-2, dolomite, illite/smectiteISCz-1 and pyrite rapidly dissolve, iii) next, quartz dissolves and greenalite crystallizes, iv) up to 5.5 moles of added iron, quartz continues to dissolve and greenalite to crystallize. From this step, quartz is nearly totally dissolved and kaolinite and saponite begin to dissolve supplying enough Si and Al to form a little ripidolite, gibbsite and always greenalite. Illite is still stable, v) illite starts to dissolve after 9 moles of iron were added. When illite is totally dissolved, formation of greenalite and gibbsite stops and magnetite crystallizes by adding more iron, vi) the final mineralogical assemblage modelled consists of greenalite, calcite, gibbsite, magnetite, pyrrhotite, and ripidolite.

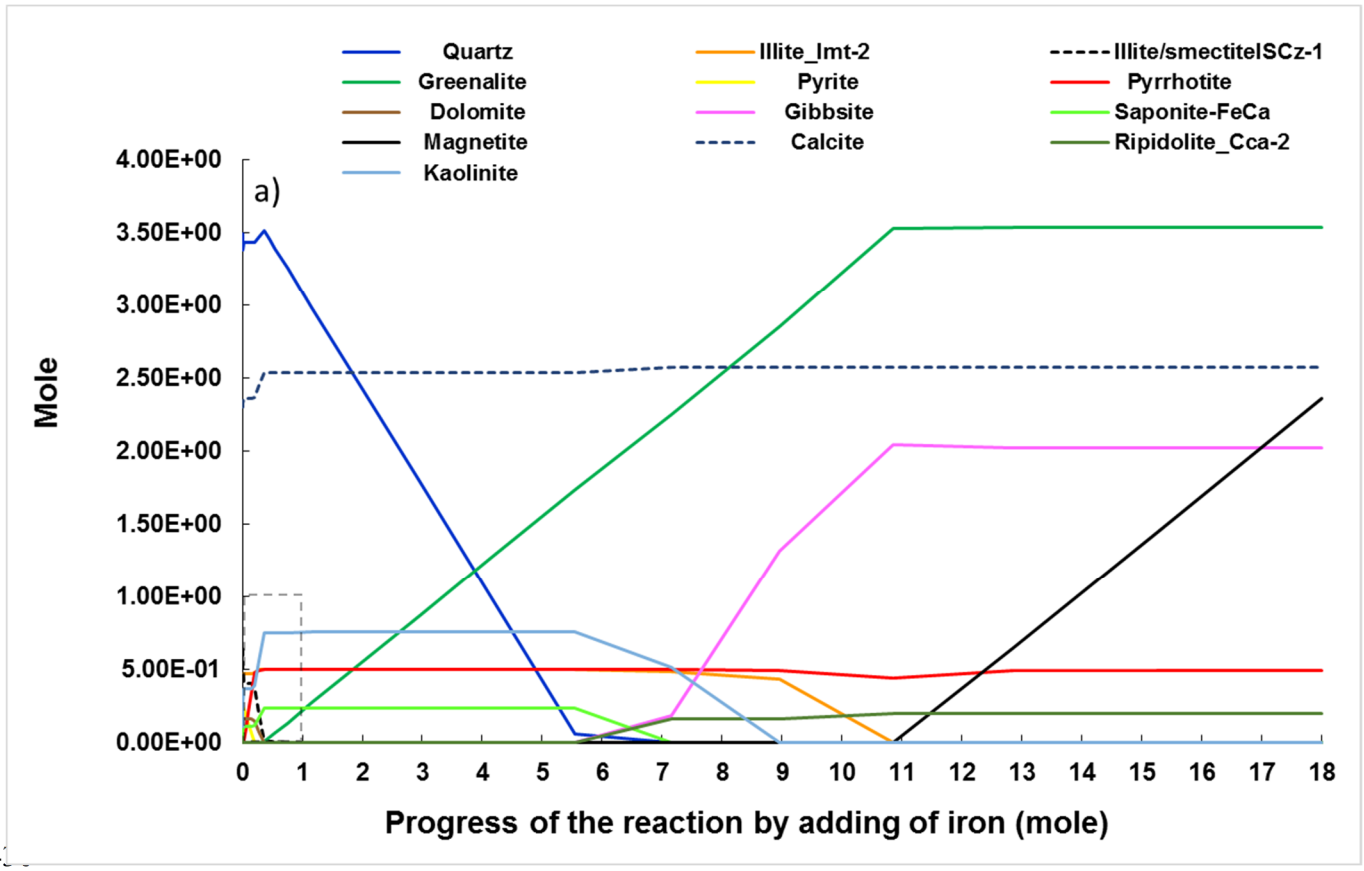
Quartz
Greenalite
Dolomite
Magnetite
Kaolinite
Illite_Imt-2
Pyrite
Gibbsite
Calcite
Illite/smectiteISCz-1
Pyrrhotite
Saponite-FeCa
Ripidolite_Cca-2
a)
Mole
4.00E+00
3.50E+00
3.00E+00
2.50E+00
2.00E+00
1.50E+00
1.00E+00
5.00E-01
0.00E+00
0 1 2 3 4 5 6 7 8 9 10 11 12 13 14 15 16 17 18
Progress of the reaction by adding of iron (mole)

431

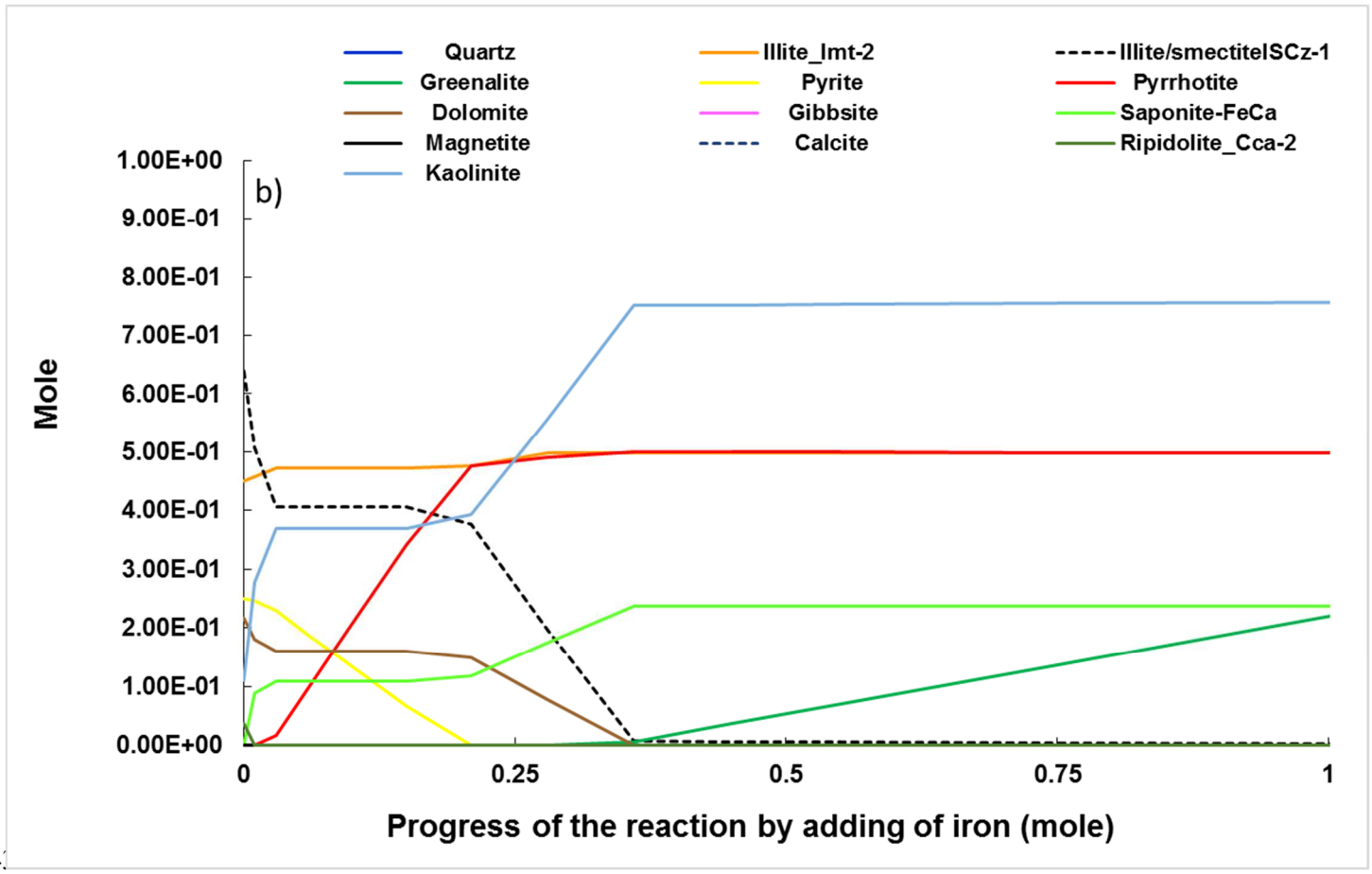
Quartz
Greenalite
Dolomite
Magnetite
Kaolinite
Illite_Imt-2
Pyrite
Gibbsite
Calcite
Illite/smectiteISCz-1
Pyrrhotite
Saponite-FeCa
Ripidolite_Cca-2
b)
Mole
1.00E+00
9.00E-01
8.00E-01
7.00E-01
6.00E-01
5.00E-01
4.00E-01
3.00E-01
2.00E-01
1.00E-01
0.00E+00
0 0.25 0.5 0.75 1
Progress of the reaction by adding of iron (mole)

433 **Fig. 9a, b:** Dissolution and crystallization of mineralogical phases versus the amount of iron
434 introduced step by step into the PHREEQC modelling. The dashed rectangle in the diagram a)
435 is zoomed in the Fig. b).

436

437 The pressure calculated at the end of the modelling, related to H_2 produced during the
438 dissolution of the metal iron added step by step (up to 17.9 moles) is around 390 bar. It is
439 much higher than that measured at the end of the experiment stopped at 107 days (around 50
440 bar). This difference can be explained by the fact that after 107 days, thermodynamic
441 equilibrium is not reached in the experiment and also because PHREEQC works with a
442 constant volume of gas, which could not be the case in the experiment because of mineral
443 transformations leading to variations of the total volume of solid phases. However
444 calculations of the volume occupied by minerals and water at the various stages of modelling
445 show that the volume occupied by these phases varies little (around 8% maximum).

446 **5. Discussion**

447 **5.1. Iron corrosion**

448 It is known that the generation of H_2 is commonly due to the anoxic corrosion of metallic iron
449 in presence of water, assuming two possible reactions (2) and (3):

450 $$2H_2O + Fe^0 \rightarrow Fe^{2+} + 2OH^- + H_{2(g)} \quad (2)$$

451 $$3H_2O + Fe^0 \rightarrow Fe^{3+} + 3OH^- + 3/2\ H_{2(g)} \quad (3)$$

452 From these equations, and using the ideal gas law, it can be predicted that only 9 to 14% of
453 iron and 4.5 to 9% of water would be consumed during the experiment to produce a partial
454 pressure of around 50 bar of H_2 measured after 107 days and assuming that the free volume
455 for gases in the reactor is that at the beginning of the experiment. However, at the end of the
456 experiment, after opening the reactor in the glove box, the reaction product appeared as a

457 solid granular mass of greenish colour and apparently dry (no liquid water was observed).
458 This result displays that the mineral transformations previously described had taken place
459 together with the iron oxidation (equations 2 and 3) and that they involve a partial dissolution
460 of some silicates and an additional water consumption. Assuming no change of the free
461 volume for gases, a relative uncertainty of 0.25 bar for gas pressure and a specific surface area
462 of the iron powder of 0.07 m^2/g (± 0.03), the initial rate of corrosion during the first ten days
463 of heating at 90°C is about 0.97 ± 0.66 $mmol/m^2/day$. This calculated initial rate of iron
464 alteration in the presence of COx is lower than the values established by Bourdelle et al.
465 (2014 and 2017) i.e. 3.66 to 9.16 $mmol/m^2/day$ and 4.5 to 11.25 $mmol/m^2/day$, respectively in
466 experiments with liquid/rock ratios of 10 or 100 and iron/rock ratios of 0.1 or 1. As the same
467 iron powder was used by these authors (same specific surface area), it appears that the initial
468 corrosion rate is very dependent on many factors as the liquid/rock mass ratio (with a strong
469 impact on ionic strength and pH in the experimental aqueous solution) and the iron/rock mass
470 ratio. The corrosion rate calculated by de Combarieu et al. (2007) in their experiment using an
471 iron/rock ratio equal to 1 but iron with a higher specific surface area (0.26 m^2/g) and a higher
472 water/rock ratio (10) is 0.52 $mmol/m^2/day$. This result compared to our data and those of
473 Bourdelle et al. (2014 and 2017) confirms that specific surface area of iron also has to be
474 considered in the evaluation of the corrosion rate of iron. Determining a kinetic law of
475 corrosion of iron over long times of experiment is therefore complex because a lot of
476 parameters have to be taken into account but are not always known or measured and
477 consequently force the authors to do some hypotheses. As a kinetic law cannot be determined
478 from the stoichiometry of a single reaction from our experiment and because the evolution of
479 the chemistry of the experimental solution is not known, the kinetics of our reaction can rather
480 be modeled from experimentally measured parameters. By continuously measuring the
481 pressure corresponding to the evolution of hydrogen content linked to the dissolution of iron,

it was possible to propose an equation for the rate of iron corrosion over the 107 days of our experiment. Assuming that the volume of the gas phase remains constant over time, the evolution of the concentration of H_2 produced during the dissolution of iron and calculated from the ideal gas law, was plotted as a function of time (Fig. 10).

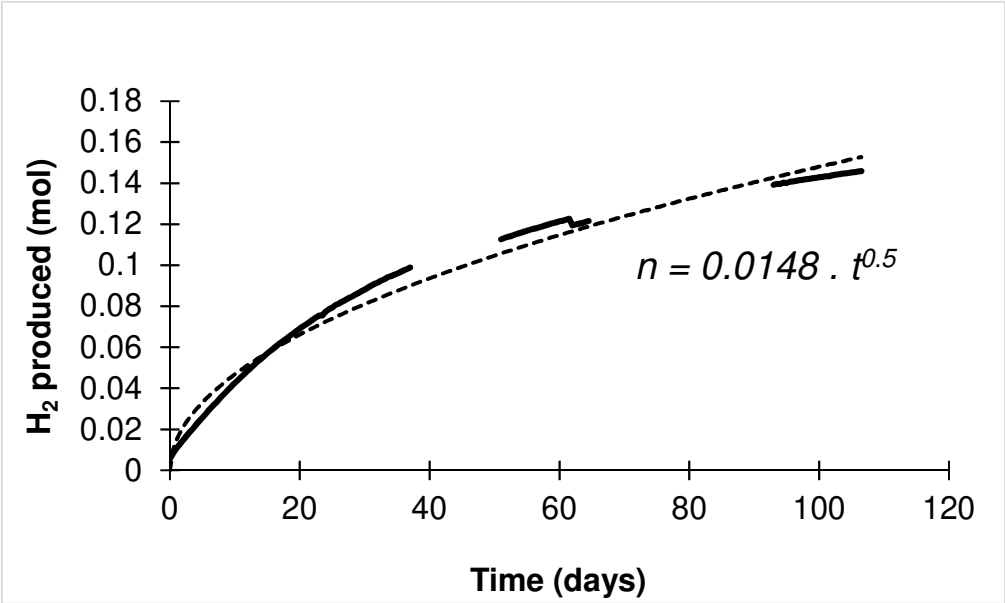

Fig. 10: Black curve: Moles of H_2 gas generated in the reactor (bar) at 90°C vs. time (days). Dotted curve is the trend curve. Its equation is $n=0.0148.t^{0.5}$.

If corrosion products develop on the surface of iron grains, the transport of corroding agents toward fresh iron can be slowed down. Diffusion could be then the rate limiting step of iron corrosion as also demonstrated by Wilson et al. (2015). These authors modelled the control of steel corrosion rate in bentonite by H_2 diffusion and showed that the rate could be decreased by two orders of magnitude. In our case, the kinetic law of H_2 production should be a function of the square root of time and written as follows: $n = k.t^{0.5}$ with n the mole number of H_2, t the time (in days) and k the rate constant (in $mol.day^{-0.5}$). Assuming a 0.5 order kinetic law, the rate of iron dissolution (r) can be deduced from the derivative of the equation $n = k.t^{0.5}$ using the same method described by Jerz and Rimstidt (2004) for pyrite oxidation: $r = dn/dt = k/2.t^{0.5}$

499 This kinetic law of dissolution of iron shows that the rate decreases when the reaction
500 progresses. The corrosion rate of iron would decrease over time because of i) the variations of
501 the proportions of the reagents and reaction products (dissolution and precipitation of
502 minerals and consequently modification of their reactive specific surface area, water
503 consumption) and/or ii) the passivation of iron due to the covering of secondary products
504 limiting the access of water to fresh iron and/or iii) the change of the pH of the solution.
505 These assumptions are supported by observed mineral transformations, both the dissolution of
506 quartz, iron, interstratified clays and illite as shown by XRD, as well as the significant
507 decrease in the amount of "free" water (*i.e.* unrelated to the crystallographic structure of
508 mineral phases produced during the experiment). The consumption of hydrogen during pyrite
509 to pyrrhotite conversion and its adsorption by clays (Didier et al., 2012) were also considered
510 to be negligible in our experiment.

511 **5.2. Precipitation of iron carbonates**

512 Under the experimental conditions presented here, *i.e.* a low $p(CO_2)$ of about 20 mbar (0.02
513 atm) developed by adding a very small initial amount of $NaHCO_3$ (about 1.2 10^{-4} mol/kgw), it
514 was a challenge to detect the presence of iron carbonates. Indeed, in other experimental
515 studies at 80°C and 90°C, thin layers of iron carbonates are always observed but the
516 concentration of $NaHCO_3$ in solutions is much higher (1 to 0.1 mol/kgw $NaHCO_3$ at pH 8.4 to
517 10 in Savoye *et al.,* 2001; 1 mol/kgw $NaHCO_3$ or 0.5 mol/kgw Na_2CO_3 at pH 9.5 in Blengino
518 *et al.*, 1995). In the experimental studies of de Combarieu (2007) and Schlegel et al. (2008),
519 the concentration of CO_2 is < 2.94 10^{-4} mol/kgw in solution, which induces a $p(CO_2)$ of 0.43
520 atm. This is the same pressure fixed by Beaucaire et al. (2012) in their thermodynamic model
521 for the prediction of pore water compositions in COx at 80°C. While the initial $p(CO_2)$ in our
522 experiment is much lower, it nevertheless corresponds to the value experimentally measured
523 at 90°C, in equilibrium with the COx carbonates and in the presence of iron (Bourdelle et al.

524 2017). As a result, its impact is weak and we can assume that the stability of calcite and, to a
525 lesser extent of the other minor carbonates of the COx, is due to the high pH of the
526 experimental solution (as predicted by modelling).

527 **5.3. Mechanisms of the mineralogical transformations**

528 The single corrosion of iron in pure water is not sufficient to explain i) the consumption of
529 water in the experimental system, ii) the granular greenish appearance of the experimental
530 reaction product and iii) the mineralogical transformations highlighted by XRD, TEM and
531 SEM, as well as Mössbauer and FTIR spectroscopies (Figs. 1 to 7). The reaction (2) in pure
532 water can be initially invoked because it quickly induces an increase of pH in the
533 experimental solution promoting the dissolution of quartz; this reaction also consumes water,
534 changes the concentration of elements (Si, Fe) and produces H_2. But other mineralogical
535 transformations also may have an indirect effect on iron corrosion. The reactions (4), (5), (6)
536 and (7) given below involve potential transformation of the COx clays into greenalite
537 ($Si_2Fe_3O_5(OH)_4$). These transformations need Fe^{2+} and may affect the corrosion of iron metal
538 and the production of H_2. The mean structural formulae of I/S and illite were calculated from
539 the analyses obtained by TEM-EDXS. Considering iron as ferrous, the mean structural
540 formula of the illite of the COx is $[Si_{3.4}Al_{0.6}](Al_{1.51}Fe^{2+}_{0.375}Mg_{0.23})O_{10}(OH)_2K_{0.83}$, which rather
541 corresponds to a phengite. The mean structural formula of I/S is
542 $[Si_{3.61}Al_{0.39}](Al_{1.40}Fe^{2+}_{0.54}Mg_{0.23})O_{10}(OH)_2K_{0.54}Ca_{0.05}$ (by ignoring the water of hydration of
543 the interlayer cations). The following reactions (4) and (5) show a consumption of Fe^{2+} and
544 water to form greenalite. Gibbsite, silica (expressed as $(SiO_2)aq$) and cations in solution are
545 by-products of these reactions. In reactions (4) and (5), Fe^{2+} in greenalite requires a prior
546 corrosion of iron metal. But it is noteworthy that the neoformation of this Fe-rich serpentine
547 mineral leads to a consumption of H_2O, additional to the moles necessary for the dissolution

of iron : another 2.17 moles of H_2O for reaction (4) and 1.77 moles of H_2O for the reaction (5).

$$[Si_{3.4}Al_{0.6}](Al_{1.51}Fe^{2+}_{0.375}Mg_{0.23})O_{10}(OH)_2K_{0.83} + 2.625\ Fe^0 + 7.42\ H_2O \rightarrow Si_2Fe_3O_5(OH)_4 +$$
Illite — Greenalite

$$1.4\ (SiO_2)aq + 2.11\ Al(OH)_3 + 0.23Mg^{2+} + 0.83K^+ + 1.29OH^- + 2.61H_{2(g)} \quad (4)$$
Gibbsite

$$[Si_{3.61}Al_{0.39}](Al_{1.40}Fe^{2+}_{0.54}Mg_{0.23})O_{10}(OH)_2K_{0.54}Ca_{0.05} + 2.46\ Fe^0 + 6.69\ H_2O \rightarrow Si_2Fe_3O_5(OH)_4$$
I/S — Greenalite

$$+ 1.61\ (SiO_2)aq + 1.79\ Al(OH)_3 + 0.23Mg^{2+} + 0.54K^+ + 0.05Ca^{2+} + 1.1OH^- + 2.45H_{2(g)} \quad (5)$$
Gibbsite

Kaolinite and chlorite (clinochlore-like) can also transform into greenalite following the reactions (6) and (7). Water and iron are also consumed. The main by-product is gibbsite as predicted by the modelling.

$$Si_2Al_2O_5(OH)_4 + 3\ Fe^0 + 6\ H_2O \rightarrow Si_2Fe_3O_5(OH)_4 + 2\ Al(OH)_3 + 3H_{2(g)} \quad (6)$$
Kaolinite — Greenalite

$$Mg_5Al(AlSi_3)O_{10}(OH_8) + 4.5\ Fe^0 + 11.5\ H_2O$$
Chlorite

$$\rightarrow 1.5\ Si_2Fe_3O_5(OH)_4 + 5\ Mg^{2+} + 10\ (OH)^- + 2\ Al(OH)_3 + 4.5\ H_{2(g)} \quad (7)$$
Greenalite — Gibbsite

The most important result highlighted by these transformation reactions of COx clays into greenalite (Eqn. (4) to (7)) is first of all a significant consumption of water. Thus, iron corrosion is not the only process that consumes water in the experiment. Furthermore, most of these reactions also produce OH^- increasing the pH in the experimental medium and consequently the dissolution of quartz. Metallic iron and silica in solution can also promote greenalite precipitation following the reaction (8) that consumes water and produces H_2 gas:

$$2\ (SiO_2)_{aq} + 3\ Fe_{(s)} + 5\ H_2O \rightarrow Si_2Fe_3O_5(OH)_4 + 3\ H_{2(g)} \quad (8)$$

As no "free" water was found that could be sampled for analysis at the end of the experiment, the hypothesis is that the water was trapped in the structure of the new clay mineral phases described above and/or adsorbed on the minerals. The processes alluded to the evolution of clay minerals towards 7 Å iron-rich clays may involve the dissolution of several layers of the starting clays (mechanism already suggested by Wilson et al. 2006a, 2006b). No cronstedtite precipitation was observed (confirmed by geochemical modelling), likely because of the excessively low water/rock ratio. Indeed, Pignatelli et al. (2014) mentioned that the crystallization of this mineral is due to a dissolution/precipitation mechanism that requires a high solution/rock mass ratio (10 in their COx-iron interaction experiments).

5.4. Modelling of the mineralogical evolution

The geochemical modelling shows some convergences and also differences with the results of the experiment. Quartz, illite and interstratified clays totally dissolve during the first steps of the modelling providing the silicon needed for greenalite to crystallize. This results is explained by the rapid increase in pH (> 10) as soon as iron is added step-by-step to the system and by the total dissolution of iron in the geochemical code. In the reaction product, a few illite and quartz still remain in the experiment (Fig. 1). Modelling also shows that magnetite can crystallize at a late stage when initial clays are totally dissolved (illite, kaolinite and I/S) and if iron is still supplied to the solution. Magnetite was not observed in our experiment maybe because there was not enough water in the medium and/or the geochemical equilibrium calculated by the code was not achieved in our experiment. De Combarieu et al. (2007) showed that magnetite was only observed after 80 days in an experimental study with Fe/COx=1 but with a higher water/rock ratio (10). Under the pe-pH conditions of the modelling (parameters free to evolve), pyrite is totally consumed to yield pyrrhotite. This is not the case in the experiment, pyrite and pyrrhotite co-exist in the reaction product as shown by SEM observations. Siderite does not crystallize in the modelling, likely because of the very

low activities of carbonate concentration in solution ($aHCO_3^-$ and $aCO_3^{2-} < 10^{-12}$ mol/kgw at pH>10), the high pH and the stability of calcite. Thus, the modelling confirms the difficulty of observing iron carbonate in the reaction product. Gibbsite is not revealed in the reaction product by the different analytical techniques used in this study. As it is shown by the modelling, it is formed at the end of the modelling, so it is supposed that in the experiment, the progress of the reaction allowing the formation of crystallized gibbsite may not have been achieved. These differences between modelling and experiment can be explained by the fact that i) the reaction kinetics are not considered in the numerical simulations, ii) the system is assumed to reach equilibrium between each step of addition of iron, iii) under the imposed experimental conditions, not all mineral phases are likely to be available to participate in chemical reactions especially at a low water/rock ratio, and iv) the difficulty of identifying newly-formed phases in a poorly crystallized mixture.

A comparison of our modelling results with other studies reveals a lot of similarities but also some divergences. Using the reaction-transport code Crunch to simulate the interactions between iron and clay-rich geological materials, Bildstein et al. (2006) show that iron oxides (magnetite) and small amounts of siderite are the main minerals of steel corrosion. Moreover, these authors confirm that the primary clay phases (illite and montmorillonite) are destabilized at the expense of iron-rich serpentine-like minerals (cronstedtite and berthierine). These authors also highlight that these mineralogical transformations may lead to significant porosity changes. Ngo et al. (2015) used the code KINDIS to simulate batch experiments on iron-claystone interactions (W/R=10 and iron/claystone=0.1), forecasting the dissolution of the more abundant primary minerals of the claystone (quartz, illite and smectite) and the formation of greenalite, chukanovite and saponite as the main secondary minerals, but without magnetite. These authors also stressed the difficulty of accurately calculating the corrosion and dissolution rates for iron, quartz and illite and, consequently, predicting the evolution of

627 pH in aqueous solution and the formation of secondary minerals. The modelling of Bildstein
628 et al. (2016) was performed using the coupled reactive transport code Crunchflow, which was
629 applied to an experimental iron-claystone (COx) interaction at 90°C for 2 years (Arcorr 2008
630 experiment described in Schlegel et al. 2014). The results of this modelling show some
631 similarities with both our experiment and modelling: i) an initial rapid increase in pH (9.5) at
632 the iron-claystone interface, ii) partial pressure (due to H_2 production) up to 40 bar, which is
633 stabilized until the end of the simulation, iii) a preferential precipitation of greenalite at the
634 surface of the iron. However, some differences also exist between the modelling of Bildstein
635 et al. (2016) and our simulation results. Magnetite and Ca-siderite are predicted as dominant
636 Fe-rich products by Crunchflow. These phases were neither observed in our experiment nor in
637 the first steps of our simulations (moreover, Ca-siderite is not in the database we used). The
638 discrepancies could be interpreted by the fact that, in our experiment and simulation, a
639 sufficient supply of silica (alteration of quartz and primary clays) would favor the
640 crystallization of greenalite at the expense of magnetite. The differences between modelling
641 studies of the literature and our own results could be due to the method we chose to introduce
642 iron into the calculation (*i.e.* step-by-step addition of iron). In addition, the stability fields of
643 hematite, magnetite and greenalite in the pe *vs.* pH phase diagram were calculated at 90°C
644 and for three values of the activity of SiO_2 in water ($aSiO_{2(aq)}=10^{-5}$ mol/kgw, 10^{-3} mol/kgw
645 and 5.10^{-4} mol/kgw). The comparison of the three phases diagrams shows that the stability
646 fields of greenalite and magnetite are present together only when $aSiO_{2(aq)}$ is equal to 5.10^{-4}
647 mol/kgw which is a value close to the solubility of quartz at 90°C (Fig. 11). The modelled
648 reaction paths (black points and black dotted line) for iron/claystone interactions under
649 hydrothermal conditions (90°C), simulated by the step-by-step addition of iron, are
650 superimposed on each other and remain within the stability field of greenalite (Fig. 11). The
651 values of pe and pH at the beginning and at the end of the modelling lead to a decimal

logarithm of oxygen fugacity ($logf_{O2}$) between -84.7 and -99.1. For these values of $logfO_2$ and assuming the solubility of quartz at 90°C, greenalite is stable as already demonstrated by Pignatelli et al (2014). The results of the characterization and modelling of the mineralogical evolution indicate that transformation of the clay fraction of the COx claystone plays a significant role in the corrosion of iron, thus supporting the assumptions of Bourdelle et al. (2017) regarding the consumption of water placed in the autoclave, and favors the increase of porosity.

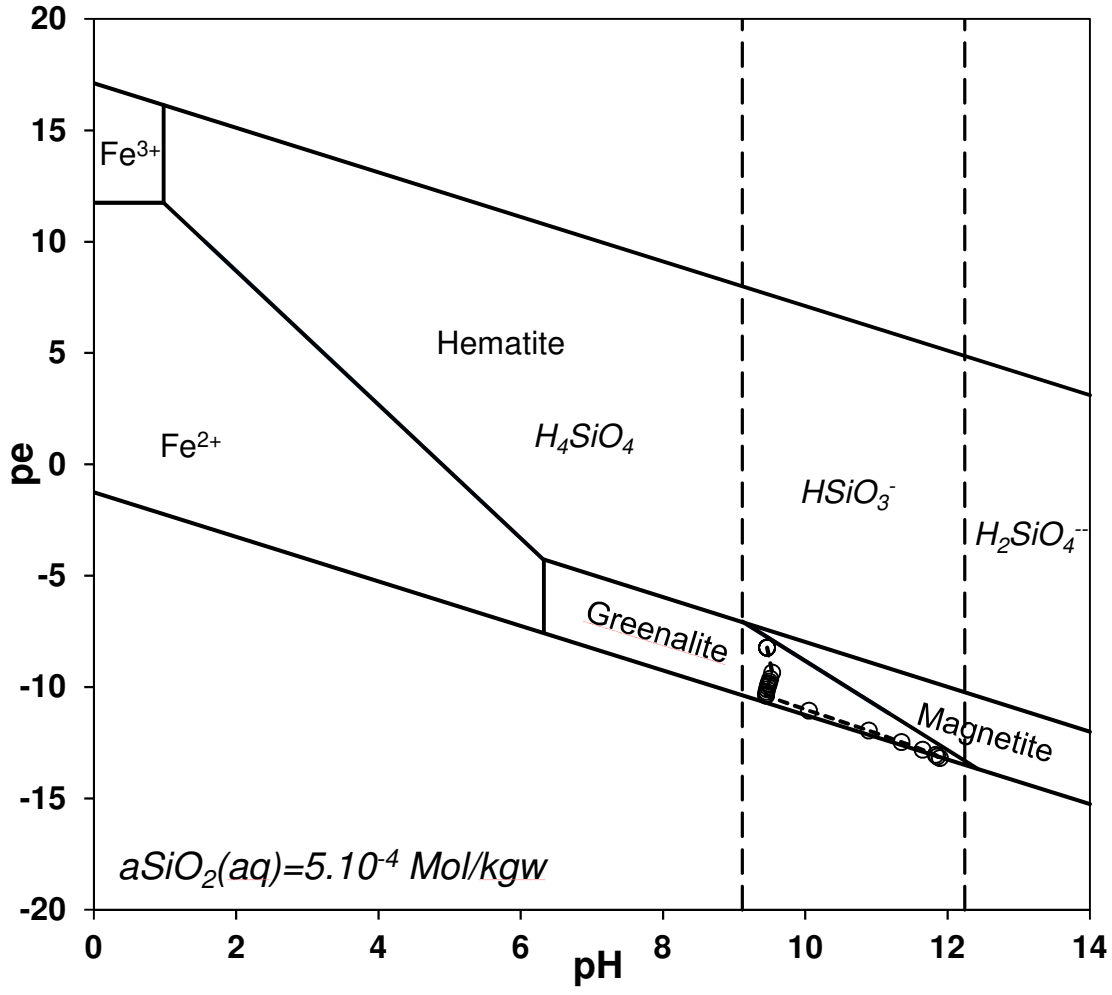

Fig. 11: Stability fields of hematite, magnetite and greenalite on pe vs. pH phase diagrams calculated at 90°C. The activity of Fe in solution is fixed at 10^{-5} mol/kgw, $p(CO_2) = 2.10^{-2}$ bar and [S] = 0 mol/kgw. Activity of $SiO_2(aq)$ is 5.10^{-4} mol/kgw. The modelling reaction path

(black points and black dotted line) for iron/claystone interactions under hydrothermal conditions (90°C) simulated by a step-by-step addition of iron is superimposed on the diagram. The PHREEQC geochemical code (Parkhurst and Appelo 1999) and the ThermoChimie_PHREEQC_SIT_v9b0 database (Giffaut et al. 2014) were used for the diagram.

Conclusion

In the presence of an initial low $p(CO_2)$ (20 mbar), the iron-claystone interaction experiment carried out at 90°C (with 1/1/1 as water/iron/rock ratio) mainly leads to the formation of iron-rich 7 Å clays with a low degree of crystallinity at the expense of the starting material made up of illite-smectite mixed-layered clays and quartz. Pyrite is altered and pyrrhotite is formed on the surface of the iron plates. The crystallization of iron hydroxycarbonate (possibly siderite or a chukanovite-like phase) in very small amounts is suspected considering the results of Mössbauer and infrared spectroscopies. Calcite remains unchanged. It is probable that pH rapidly rises above at least 9 at the beginning of the experiment leading to the dissolution of quartz. This increase of pH is due to the corrosion of iron by water. The water consumption observed at the end of the experiment and the production of H_2 are explained by both the corrosion of iron and mineralogical reactions such as the transformation of illite and I/S into newly-formed 7Å iron-rich clays (greenalite-like) and the likely formation of hydrated amorphous hydroxides. Magnetite is not observed under our experimental conditions. However, the transformations and crystallinity of the reaction minerals are likely limited by the small quantity of water in the experimental system. Since the experiment presented here was carried out under a low $p(CO_2)$, the impact of CO_2 on mineral transformations is also difficult to estimate, the gaseous phase of the experimental system being largely dominated by H_2. A very low oxygen fugacity is indicated by the presence of

688 sparse iron carbonates and pyrrhotite crystallized on the surface of the iron plates, together
689 with iron-rich clays with a composition lying along a trend between I/S and greenalite. This
690 study confirms that water/rock and water/iron ratios remain very sensitive parameters which
691 must be taken into account to understand the reactivity of the COx in contact with steel
692 containers. The most important result is the demonstration that, during the iron-claystone
693 interaction experiments, water consumption is not only due to iron corrosion but also to
694 mineralogical transformations and, in particular, the formation of Fe-serpentine. This
695 consumption of water will have an impact on the hydration state of the claystone and
696 necessarily on the long term behaviour of this geological barrier in the high-level radioactive
697 wastes repositories.
698
699 **Acknowledgments**
700 The discussions and comments of the journal editor and of the two anonymous reviewers are
701 gratefully acknowledged. The authors also thank L. Salsi for the acquisition of SEM images
702 and J. Ghanbaja for TEM analyses at the SCMEM and IJL laboratories (Université de
703 Lorraine, France). The research was financially supported by Andra (French national agency
704 for the management of radioactive waste). M.S.N. Carpenter post-edited the English style and
705 grammar.
706
707 **References:**
708
709 Allen DE, Seyfried WEJ (2003) Compositional controls on vent fluids from ultramafic-hosted
710 hydrothermal systems at mid-ocean ridges: an experimental study at 400°C, 500 bars.
711 Geochim Cosmochim Acta 67:1531-1542
712

713 Andreani M, Muñoz M, Marcaillou C, Delacour A (2013) μXANES study of iron state in
714 serpentine during oceanic serpentinization. Lithos 178:70-83
715
716 Azoulay I, Rémazeilles C, Refait P (2012) Determination of standard Gibbs free energy of
717 formation of chukanovite and Pourbaix diagrams of iron in carbonated media. Corros Sci
718 58:229-236. DOI 10.1016/j.corsci.2012.01.033
719
720 Beaucaire C, Tertre E, Ferrage E, Grenut B, Pronier S, Madé B (2012) A thermodynamic
721 model for the prediction of pore water composition of clayey rock at 25°C and 80°C –
722 Comparison with results from hydrothermal alteration experiments. Chem Geol 334:62-76
723
724 Bildstein O, Trotignon L, Perronnet M, Jullien M (2006) Modelling iron-clay interactions in
725 deep geological disposal conditions. Phys Chem Earth 31:618-625
726
727 Bildstein O, Lartigue J E, Schlegel ML, Bataillon C, Cochepin B, Munier I, Michau N (2016)
728 Gaining insight into corrosion processes from numerical simulations of an integrated iron-
729 claystone experiment. From Norris S, Bruno J, Van Geet M and Verhoef E (eds) Radioactive
730 Waste Confinement: Clays in Natural and Engineered Barriers. Geological Society, London,
731 Special Publications 443. http://doi.org/10.1144/SP443.2
732
733 Blengino JM, Keddam M, Labbe JP, Robbiola L (1995) Physico-chemical characterization of
734 corrosion layers formed on iron in a sodium carbonate-bicarbonate containing environment.
735 Corros Sci 34, 4:621-643
736

737 Bourdelle F, Truche L, Pignatelli I, Mosser-Ruck R, Lorgeoux C, Roszypal C, Michau N
738 (2014) Iron–clay interactions under hydrothermal conditions: Impact of specific surface area
739 of metallic iron on reaction pathway. Chem Geol 381:194-205
740
741 Bourdelle F, Mosser-Ruck R, Truche L, Lorgeoux C, Pignatelli I, Michau N (2017) A new
742 view on iron-claystone interactions under hydrothermal conditions (90°C) by monitoring in
743 situ pH evolution and H_2 generation. Chem Geol 466:600-607
744
745 Charlou JL, Donval JP, Fouquet Y, Jean Baptiste P, Holm N (2002) Geochemistry of high H_2
746 and CH_4 vent fluids issuing from ultramafic rocks at the Rainbow hydrothermal field
747 (36_14'N, MAR). Chem Geol 191:345-359
748
749 Didier M, Leone L,Greneche JM, Giffaut E, Charlet L (2012) Adsorption of Hydrogen Gas
750 and Redox Processes in Clays**.** Environ Sci Technol (2012) 46 (6) : 3574–3579. DOI**:**
751 10.1021/es204583h
752
753 Douville E, Charlou JL, Oelkers EH, Bianvenu P, Jove Colon CF, Donval JP, Fouquet Y,
754 Prieur D, Appriou P (2002) The Rainbow vent fluids (36_14'N, MAR): the influence of
755 ultramafic rocks and phase separation on trace metal contents on Mid-Atlantic Ridge
756 hydrothermal fluids. Chem Geol 184:37-48
757
758 de Combarieu G (2007) Altération du verre de confinement de déchets type R7T7 en
759 condition de stockage géologique. PhD Thesis Univ Paris XI, Orsay, France
760

761 de Combarieu G, Barboux P, Minet Y (2007) Iron corrosion in Callovo-Oxfordian argilite :
762 From experiments to thermodynamic/kinetic modelling. Phys Chem Earth 32:346-358
763
764 de Combarieu G, Schlegel ML, Neff D, Foy E, Vantelon D, Barboux P, Gin S (2011) Glass-
765 iron-clay interactions in a radioactive waste geological disposal: An integrated laboratory-
766 scale experiment. Appl Geochem 26:65-79
767
768 Farmer VC (1974) The layer silicates. Pp. 331_363 in: The Infrared Spectra of Minerals (V.C.
769 Farmer, editors). Monograph 4, Mineralogical Society, London
770
771 Foustoukos DJ, Savoy LP, Janecky DR (2008) Chemical and isotopic constraints on
772 water/rock interactions at the Lost City hydrothermal field, 30_N Mid-Atlantic Ridge.
773 Geochim Cosmochim Acta 72:5457-5474
774
775 Früh-Green GL, Kelley DS, Bernasconi SM, Karson JA, Ludwig KA, Butterfiled DA, Boschi
776 C, Proskurowski G (2003) 30,000 years of hydrothermal activity at the Lost City vent field.
777 Science 301:495-498
778
779 Fu Q, Sherwood Lollar B, Horita J, Lacrampe-Couloume G, Seyfried Jr WE (2007) Abiotic
780 formation of hydrocarbons under hydrothermal conditions: constraints from chemical and
781 isotope data. Geochim Cosmochim Acta 71:1982-1998
782
783 Gailhanou H, Lerouge C, Debure M, Gaboreau S, Gaucher EC, Grangeon S, Grenèche JM,
784 Kars M, Madé B, Marty NCM, Warmont F, Tournassat C (2017) Effects of a thermal

785 perturbation on mineralogy and pore water composition in a clay-rock: an experimental and
786 modelling study. Geochim Cosmochim Acta 197:193-214
787
788 Gaucher E, Robelin C, Matray JM, Negrel G, Gros Y, Heitz JF, Vinsot A, Rebours H,
789 Casagnabère A, Bouchet A (2004) ANDRA underground research laboratory: interpretation
790 of the mineralogical and geochemical data acquired in the Callovo-Oxfordian formation by
791 investigative drilling. Phys Chem Earth 29:55-77
792
793 Gaucher E C, Tournassat C, Pearson F J, Blanc P, Crouzet C, Lerouge C, Altmann S (2009) A
794 robust model for pore-water chemistry of clayrock. Geochim Cosmochim Acta 73: 6470-6487
795 Gaucher EC, Lassin A, Lerouge C, Fléhoe C, Marty N, Henry B, Tournassat C, Altmann S,
796 Vinsot A, Buschaert S, Matray J M, Leupin O, De Craen M (2010) CO_2 partial pressure in
797 clayrocks: a general model. Water-Rock Interaction WRI-13, Guanajuato, Mexico: 855-858,
798 hal-00664967
799
800 Giffaut E, Grivé M, Blanc P, Vieillard P, Colàs E, Gailhanou H, Gaboreau S, Marty N, Madé
801 B, Duro L (2014) Andra thermodynamic database for performance assessment:
802 ThermoChimie. Appl Geochem 49:225-236
803
804 Guillaume D, Neaman A, Cathelineau M, Mosser-Ruck R, Peiffert C, Abdelmoula M,
805 Dubessy J, Villiéras F, Baronnet A, Michau N (2003) Experimental synthesis of chlorite from
806 smectite at 300° C in the presence of metallic Fe. Clay Miner 38:281-302
807

808 Guillaume D, Neaman A, Cathelineau M, Mosser-Ruck R, Peiffert C, Abdelmoula M,
809 Dubessy J, Villiéras F, Baronnet A, Michau N (2004) Experimental study of the
810 transformation of smectite at 80 and 300°C in the presence of Fe oxides. Clay Miner 39:17-34
811
812 Jerz JK, Rimstidt JD (2004) Pyrite oxidation in moist air. Geochim Cosmochim Acta 68,
813 701:714
814
815 Jodin-Caumon MC, Mosser-Ruck R, Randi A, Cathelineau M, Michau N (2010) Iron-Clay
816 interactions under various H_2 pressures. Clays in Natural and Engineered Barriers for
817 Radioactive Waste Confinement, Nantes 2010, 4th International Meeting
818
819 Jodin-Caumon MC, Mosser-Ruck R, Randi A, Pierron O, Cathelineau M, Michau N (2012)
820 Mineralogical evolution of a claystone after reaction with iron under thermal gradient. Clay
821 Clay Miner 60:443-455
822
823 Kaufhold S., Hassel AW, Sanders D, Dohrmann R (2015) Corrosion of high-level radioactive
824 waste iron-canisters in contact with bentonite. J Hazard Mater 285: 464-473
825
826 Kaufhold S, Dohrmann R (2016) Distinguishing between more and less suitable bentonites
827 for storage of high-level radioactive waste. Clay Miner 51(2): 289-302
828
829 Kelley DS, Karson JA, Früh-Green GL, Yoerger DR, Shank TM, Butterfield DA, Hayes JM,
830 Schrenk MO, Olson EJ, Proskurowski G, Jakuba M, Bradley A, Larson B, Ludwig K,
831 Glickson D, Buckman K, Bradley AS, Brazelton WJ, Roe K, Elend MJ, Delacour A,

832 Bernasconi SM, Lilley MD, Baross JA, Summons RE, Sylva SP (2005) A serpentinite-hosted
833 ecosystem: the Lost City hydrothermal field. Science 307 (5714):1428-1434
834
835 Klein F, Bach W, Jöns N, McCollom T, Moskowitz B, Berquo T (2009) Iron partitioning and
836 hydrogen generation during serpentinization of abyssal peridotites from 15_N on the Mid-
837 Atlantic Ridge. Geochim Cosmochim Acta 73:6868-6893
838
839 Kohn T, Livi K, Roberts AL, Vikesland P (2005) Longevity of granular iron in groundwater
840 treatment processes: corrosion product development. Environ Sci Technol 39:2867-2879
841
842 Lanson B, Lantenois S, Van Aken PA, Bauer A, Plançon A (2012) Experimental investigation
843 of smectite interaction with metal iron at 80°C: structural characterization of newly formed
844 Fe-rich phyllosilicates. Am Mineral 97:864-871
845
846 Lantenois S, Lanson B, Muller F, Bauer A, Jullien M, Plançon A (2005) Experimental study
847 of smectite interaction with metal Fe at low temperature: 1-smectite destabilization. Clays and
848 Clay Miner 53:597-612
849
850 Lee TR, Wilkin RT (2010) Iron hydroxyl carbonate formation in zerovalent iron permeable
851 reactive barriers: Characterization and evaluation of phase stability. Journal of Contaminant
852 Hydrology 116:47-57. DOI 10.1016/j.jconhyd.2010.05.009
853
854 Marcaillou C, Muñoz M, Vidal O, Parra T, Harfouche M (2011) Mineralogical evidence for
855 H_2 degassing during serpentinization at 300°C/300 bar. Earth and Planet Sci Letters 303:281-
856 290

MacCollom TM, Bach W (2009) Thermodynamic constraints on hydrogen generation during serpentinization of ultramafic rocks. Geochim Cosmochim Acta 73:856-875

Martin FA, Bataillon C, Schlegel ML (2008) Corrosion of iron and low alloyed steel within a water saturated brick of clay under anaerobic deep geological disposal conditions: An integrated experiment. J Nucl Mater 379:80-90

Moëlo Y, Léone P, Matsushita Y, Mancini-Le Granvalet M, Deniard P (2009) Berthiérine hydrothermale de Saint Aubin des Châteaux. April 4-16 th, 7^{e} colloque GFA, Toulouse, France

Mosser-Ruck R, Cathelineau M, Guillaume D, Charpentier D (2010) Effects of temperature, pH, and iron/clay and liquid/clay ratios on experimental conversion of dioctahedral smectite to berthierine, chlorite, vermiculite, or saponite. Clays Clay Miner 58:280-291

Mosser-Ruck R, Pignatelli I, Bourdelle F, Abdelmoula M, Barres O, Guillaume D, Charpentier D, Rousset D, Cathelineau M, Michau N (2016) Contribution of long-term hydrothermal experiments for understanding the smectite-to-chlorite conversion in geological environments. Contrib Miner Petrol 171 (11):1-21. DOI 10.1007/s00410-016-1307-z

Musić S, Nowik I, Ristić M, Orehovec Z, Popović S (2004) The effect of bicarbonate/carbonate ions on the formation of iron rust. Croatia Chemica Acta, CCACCA77 (1-2):141-151

881

882 Ngo VV, Clément A, Michau N, Fritz B (2015) Kinetic modelling of interactions between
883 iron and water: Comparison with data from batch experiments. Appl Geochem 53:13-26

884

885 Nishimura T, Dong J (2009) Corrosion behaviour of carbon steel for overpack in groundwater
886 containing bicarbonate ions. J Power Energy Syst 3 (1):23-30. DOI 10.1299/jpes.3.23

887

888 Osaký M, Śucha V, Czímerová A, Madejová J (2010) Reaction of smectites with iron in a
889 nitrogen atmosphere at 75°C. Appl Clay Sci 50:237-244

890

891 Parkhurst DL, Appelo CAJ (1999) User's Guide to PHREEQC (Version 2). A Computer
892 Program for Speciation, Batch-reaction, One-dimensional Transport, and Inverse
893 Geochemical Calculations. US Geol Surv Water Resour Inv Rep 99-4259, Pp. 312

894

895 Perronnet M, Jullien M, Villiéras F, Raynal J, Bonnin D, Bruno G (2008) Evidence of a
896 critical content in Fe(0) on FoCa7 bentonite reactivity at 80°C. Appl Clay Sci 38:187-202

897

898 Pierron O (2011) Interactions eau-fer-argilite : Rôle des paramètres Liquide/Roche,
899 Fer/Argilite, Température sur la nature des phases minérales. Université Henri Poincaré,
900 Nancy, France, PhD Thesis, Pp 230

901

902 Pignatelli I, Mugnaioli E, Hybler J, Mosser-Ruck R, Cathelineau M, Michau N (2013) A
903 multi-technique characterisation of cronstedtite synthetised by iron-clay interaction in a step-
904 by-step cooling procedure. Clay Miner 61:277-289

905

906 Pignatelli I, Mugnaioli E, Mosser-Ruck R, Barres O, Kolb U, Michau N (2014a) A multi-
907 technique description from micrometric to atomic scale of a sunthetic analog of chukanovite,
908 $Fe_2(CO_3)(OH)_2$. Eur J Min 26 (2):221-229
909
910 Pignatelli I, Bourdelle F, Bartier D, Mosser-Ruck R, Truche L, Mugnaioli E, Michau N
911 (2014b) Iron-clay interactions: Detailed study of the mineralogical transformation of
912 claystone with emphasis on the formation of iron-rich T-O phyllosilicates in a step-by-step
913 cooling experiment from 90°C to 40°C. Chem Geol 387:1-11
914
915 Pignatelli I, Marrocchi Y, Vacher L, Delon R (2016) Multiple precursors of secondary
916 mineralogical assemblages in CM chondrites. Meteor Planet Sci 51 (4):785-805. doi:
917 10.1111/maps.12625
918
919 Pignatelli I, Marrocchi Y, Mugnaioli E, Bourdelle F, Gounelle M (2017) Mineralogical,
920 crystallographic and redox features of the earliest stages of fluid alteration in CM chondrites.
921 Geochim Cosmochim Acta 209:106–122
922
923 Refass M, Sabot R, Savall C, Jeannin M, Creus J, Refait P (2006) Localised corrosion of
924 carbon steel in $NaHCO_3$/NaCl electrolytes: role of Fe(II)-containing compounds. Corros Sci
925 48:709-726
926
927 Rémazeilles C, Refait P (2009) Fe(II) hydroxycarbonate $Fe_2(OH)_2CO_3$ (chukanovite) as iron
928 corrosion product: synthesis and study by Fourier transform infrared spectroscopy.
929 Polyhedron 28:749-756

930 Rivard C (2011) Contribution à l'étude de la stabilité des minéraux constitutifs de l'argilite du
931 Callovo-Oxfordien en présence de fer à 90° C. Institut National Polytechnique de Lorraine.
932 PhD Thesis 338 Pp
933
934 Rivard C, Pelletier M, Michau N, Razafitianamaharavo A, Abdelmoula M, Ghanbaja J,
935 Villieras F (2015) Reactivity of Callovo-Oxfordian claystone and its clay fraction with
936 metallic iron: Role of non-clay minerals on the mechanism of interaction. Clays and clay
937 miner 63 (4):290-310
938
939 Rousset D (2001) Etude de la fraction argileuse de séquences sédimentaires de la Meuse et
940 du Gard. Reconstitution de l'histoire diagénétique et des caractéristiques physico-chimiques
941 des cibles. Aspects minéralogiques, géochimiques et isotopiques. Université Louis Pasteur,
942 Strasbourg, France, PhD Thesis, 270 Pp.
943
944 Ruhl AS, Kotré C, Gernert U, Jekel M (2011) Identification, quantification and localization of
945 secondary minerals in mixed Fe^0 fixed bed reactors. Chem Eng J 172:811-816
946
947 Saheb M, Neff D, Dillmann P, Matthiesen H, Foy E (2008) Long-term behavior of low-
948 carbon steel in anoxic environment: Characterization of archaeological artefacts. J Nucl Mater
949 379:118-123
950
951 Saheb M, Neff D, Dillmann P, Matthiesen H, Foy E, Bellot-Gurlet L (2009) Multisecular
952 corrosion behavior of low carbon steel in anoxic soils: Characterization of corrosion system
953 on archaeological artefacts. Mater and Corros 60 (2):99-105
954

955 Saheb M, Descotes M, Neff D, Matthiesen H, Michelin A, Dillmann P (2010) Iron corrosion
956 in an anoxic soil: Comparison between thermodynamic modelling and ferrous archaeological
957 artefacts characterized along with the local in situ geochemical conditions. Appl Geochem 25:
958 1937-1948
959
960 Saheb M, Neff D, Bellot-Gurlet L, Dillmann P (2011) Raman study of a deuterated iron
961 hydroxycarbonate to assess long-term corrosion mechanisms in anoxic soils. J of Raman
962 Spectrosc 42:1100-1108. DOI 10.1002/jrs.2828
963
964 Savoye S, Legrand L, Sagon G, Lecomte S, Chausse A, Messina R, Toulhoat P (2001)
965 Experimental investigations of iron corrosion products formed in bicarbonate/carbonate-
966 containing solutions at 90°C. Corros Sci 43 (11):2049-2064
967
968 Schlegel ML, Bataillon C, Benhamida K, Blanc C, Menut D, Lacour JL (2008) Metal
969 corrosion and argillite transformation at the water-saturated, high-temperature iron-clay
970 interface: A microscopic-scale study. Appl Geochem 23:2619-2633
971
972 Schlegel ML, Bataillon C, Blanc C, Prêt D, Eddy F (2010) Anodic activation of iron in clay
973 media under water-saturated conditions at 90°C: Characterisation of the corrosion interface.
974 Environ Sci Technol 44:1503-1508
975
976 Schlegel ML, Bataillon C, Brucker F, Blanc C, Prêt D, Foy E, Chorro M (2014) Corrosion of
977 metal iron in contact with anoxic clay at 90°C: characterization of the corrosion products after
978 two years of interaction. Appl Geochem 51:1-14
979

980 Schlegel ML, Martin F, Fenart M., Blanc C, Varlet J, Foy E, Prêt D, Trcera N (2019)
981 Corrosion at the carbon steel-clay compact interface at 90°C: insight into short- and long-term
982 corrosion facies. Corros Sci 152: 31-44
983
984 Seyfried WEJ, Foustoukos DI, Fu Q (2007) Redox evolution and mass transfer during
985 serpentinization: an experimental and theoretical study at 200°C, 500 bar with implications
986 for ultramafic-hosted hydrothermal systems at mid-ocean ridges. Geochim Cosmochim Acta
987 71: 3372–3886.
988
989 Truche L, Jodin-Caumon MC, Lerouge C, Berger G, Mosser-Ruck R, Giffaut E, Michau N
990 (2013) Sulphide mineral reactions in clay-rich rock induced by high hydrogen pressure
991 Application to disturbed or natural settings up to 250°C and 30 bar. Chem Geol 351:217-228
992
993 Wilson J, Cressey G, Cressey B, Cuadros J, Ragnarsdottir KV, Savage D, Shibata M (2006a)
994 The effect of iron on montmorillonite stability. (II) Experimental investigation Geochim
995 Cosmochim Acta 70:323-336
996
997 Wilson J, Savage D, Cuadros J, Shibata M, Ragnarsdottir KV (2006b) The effect of iron on
998 montmorillonite stability. (I) Background and thermodynamic considerations Geochim
999 Cosmochim Acta 70:306-322
1000
1001 Wilson J, Benbow S, Sasamoto H, Savage D, Watson C (2015) Thermodynamic and fully-
1002 coupled reactive transport of a steel-bentonite interface. App Geochem 61:10-28